Title
Recent progress in iron oxide based photoanodes for solar water splitting

Journal
Journal of Physics D, 51(47)

ISSN
0022-3727

Authors
Gurudayal
Bassi, Saurabh
Sritharan, Thirumany
et al.

Publication Date
2018-11-28

DOI
10.1088/1361-6463/aae138

Journal of Physics D: Applied Physics

TOPICAL REVIEW

Recent progress in iron oxide based photoanodes for solar water splitting

To cite this article: Gurudayal *et al* 2018 *J. Phys. D: Appl. Phys.* **51** 473002

IOP Publishing

Journal of Physics D: Applied Physics

J. Phys. D: Appl. Phys. **51** (2018) 473002 (28pp)

https://doi.org/10.1088/1361-6463/aae138

Topical Review

Recent progress in iron oxide based photoanodes for solar water splitting

Gurudayal[1,2], **Prince Saurabh Bassi**[1,3], **Thirumany Sritharan**[1] and **Lydia Helena Wong**[1,4]

[1] School of Materials Science and Engineering, Nanyang Technological University, 50 Nanyang Avenue, Singapore 639798, Singapore

[2] Joint Center for Artificial Photosynthesis and Chemical Sciences Division, Lawrence Berkeley National Laboratory, Berkeley, CA 94720, United States of America

[3] Helmholtz-Zentrum Berlin für Materialien und Energie GmbH, Institute for Solar Fuels, Hahn-Meitner-Platz 1, Berlin 14109, Germany

E-mail: lydiawong@ntu.edu.sg

Received 10 August 2017, revised 23 July 2018
Accepted for publication 13 September 2018
Published 17 October 2018

Abstract

Solar assisted water splitting in a PEC is an attractive concept to store solar energy as hydrogen fuel but the effective efficiency of the process is too low for it to be a serious contender for commercialization. The most important component of the PEC to achieve efficient water splitting is a photo active anode that could effectively absorb photons and deliver holes for the oxygen evolution reaction. Hematite has many attributes that make it a good candidate material for a photoanode but it also has some deficiencies. This article reviews the state-of-the-art hematite-based photoanodes, with special emphasis on attempts made by researchers to overcome its drawbacks. The numerous research reports are categorized under distinct strategies such as nanostructuring, elemental doping, surface passivation, cocatalyst application, conducting template incorporation and heterostructures which are possible pathways to improve the performance of hematite. The scientific understandings of the operating mechanisms for each strategy are systematically presented and discussed, and the improvements achieved by different approaches are compared. Some cutting-edge strategies, such as heterojunctions, could be important and hematite based heterostructures are discussed. A developing interest in an emerging material, Fe_2TiO_5 is also discussed and some of the important benefits of this material are presented. Finally, the importance of scaling up the technology is discussed and attention is drawn to some possible challenges on scaling up. The paper concludes with some future technology directions and prospects for hematite-based photoanodes.

Keywords: hematite, iron titanate, iron oxide, solar water splitting, artificial photosynthesis, bulk and surface recombinations, Fe_2O_3

(Some figures may appear in colour only in the online journal)

[4] Author to whom any correspondence should be addressed.

1. Introduction

Rapid economic and demographic growth have been driving the upsurge in worldwide energy consumption. To date, fossil fuels continue to meet more than 80% of the total primary energy demand and over 90% of greenhouse gas emissions [1, 2]. One of the most abundant sources of clean energy, solar energy, is freely available on earth surface, however, the main challenge is to convert and store solar energy by efficient and cost effective methods on a large scale. Solar driven water splitting is an interesting pathway to harvest solar energy and generate hydrogen gas, mimicking the first stage of the natural photosynthesis process in plants, where solar energy is captured and ultimately converted to carbohydrates evolving oxygen [3–5]. In a photoelectrochemical (PEC) cell, water molecules are broken into hydrogen on the surface of photocathode, and oxygen on the surface of a photoanode. Ideal photoanode/cathode materials should have a suitable energy bandgap for sunlight harvesting, appropriate band edges with water redox reactions, high absorption in visible wavelength range, good electrical conductivity, good chemical stability, nontoxicity, and economic viability [6, 7]. For the purpose of optimizing the photoanode/cathode stack, the other electrode might be replaced with a counter electrode made of Platinum to form a half PEC cell. Compared to the H_2 evolution reaction at the photocathode, the four-electron transfer oxygen evolution reaction (OER) at the photoanode is the rate-limiting step in the PEC water splitting process, thus the development of high-efficiency photoanodes is of paramount importance.

After the pioneering work of Fujishima and Honda on TiO_2 photoanodes for PEC water splitting, various other photoactive materials such as Fe_2O_3, WO_3, $BiVO_4$, TaON, GaP, GaInP, np$^+$-Si, and Ta_3N_5 have been examined for anode [8–13]. Metal oxides are a common choice for photoanode material mainly due to their semiconducting nature, chemical stability in aqueous solutions and reasonably low cost [6]. However, most metal oxides have wide energy bandgaps and poor electrical properties (carrier concentrations and mobilities) when compared with traditional III–V semiconductors and silicon.

The US Department of Energy estimates the hydrogen threshold cost to be \$2.00–\$4.00 per gallon [14], while a recent report predicts the cost of hydrogen production via electrolysis to be \$3.26–\$6.62 per gallon [15]. To meet the DOE cost target, a PEC device should cost less than US\$ 160 per m^2 with a solar-to-hydrogen (STH) efficiency of about10% [16] whereas the theoretical maximum efficiency of most of the metal oxide based photoanodes is still below 15% based on their energy band gap (see table 1 below).

Among metal oxide photoanodes, TiO_2 has received considerable attention due to its energy band offsets, but its high energy band gap and inefficient absorption of visible spectrum have limited its performance [26]. The performance of bismuth vanadate ($BiVO_4$) has been improved in recent years by surface and bulk modifications and has reached 80.7% of its theoretically predicted STH efficiency [11, 21, 27]. However its poor stability in the electrolyte environment remains to beaddressed. WO_3 is another oxide that has been investigated widely but it exhibits poor performance and is not stable in alkaline conditions frequently used in PEC [10]. np$^+$-Si photoabsorber integrated with various co-catalysts shows excellent PEC water oxidation performance but it also requires a protection layer to guard against corrosion [12]. Oxynitrides, which can undergo both water oxidation and reduction, are also widely studied because of their suitable energy band gap but their reported quantum efficiency (~5%–6%) is still too low [28, 29]. Out of all the candidate materials, hematite (Fe_2O_3) seems to have the most favorable properties of high theoretical STH efficiency and stability [24, 30].

Hematite (α-Fe_2O_3), is a naturally occurring ore of iron which is the fourth most abundant element in earth's crust (6.3% by weight) [31, 32]. It has many desirable characteristics of a good photoanode material such as good chemical stability in aqueous media, suitable energy band gap (1.9–2.2 eV) for light harvesting, low cost and environment friendliness [33]. Based on its energy bandgap, hematite can achieve a theoretical maximum STH efficiency of 15%, which exceeds the STH benchmark efficiency of 10% forecast for commercial applications [33, 34]. However, in practice, its performance is limited by low carrier concentration, poor electronic properties and slow charge transfer kinetics at electrode/electrolyte interface leading to a high overpotential for water oxidation and a lower than the predicted STH efficiency [33, 35]. Several reviews have been published highlighting significant achievements made in improving hematite photoanode performance using various approaches. In our previous review article, we discussed various nanostructures, doping strategies and surface modifications examined in hematite photoanodes with an aim of enhancement of charge carrier dynamics in PEC water splitting. Significant progress has been made on improving the performance of hematite photoanode since 1978 (figure 1). A recent report by Wonyong Choi's group reveals 6 mA cm^{-2} current density at 1.23 V versus RHE, which is ~50% of the theoretically predicted photocurrent density based on the energy band gap [30]. However, further improvement of hematite performance still has to be pursued by alternative strategies, such as by fabricating heterostructures to incorporate a second material to promote charge separation, charge collection, and surface catalysis. In this review, we summarize recent efforts to understand and realize the potential of hematite photoanode and discuss possible strategies to address the outstanding challenges.

2. Hematite (Fe_2O_3) photoanodes

As a potential photoanode material with excellent stability, hematite has an appropriate valence band for water oxidation (figure 2) [33, 34, 40] even though the conduction band minima is not pertinent for water redox level [43]. Figure 2 shows the band offsets of hematite before and after interaction with an electrolyte. The use of hematite in thin film or bulk forms is not successful because of the competing requirement between its low minority carrier diffusion length (2–10 nm) and its need for high absorption depth (~120 nm at 550 nm wavelength) to convert significant amount of incident energy

Table 1. Solar to hydrogen conversion (STH) efficiency of various photoanodes.

Photoanode Materials	Energy Band Gap (eV)	Theoretical STH (%)	Reported STH (%)	References
TiO_2 (anatase)	3.2	1.3	0.098	[17, 18]
TiO_2 (rutile)	3.0	2.2	0.6	[17, 19]
$BiVO_4$	2.4	9.1	6.2	[20, 21]
WO_3	2.7	4.8	3.0	[22, 23]
Fe_2O_3	2.2	15	3.4	[20, 24]
TaON	2.4	9.1	Not reported	[17]
Ta_3N_5	2.1	16	Not reported	[17]
Fe_2TiO_5	2.1	16	Not reported	[25]

[33, 44]. Because of the low hole diffusion length, only holes generated within a few nanometers of the hematite electrolyte-interface can be useful for water oxidation.

A good photoanode should have a high plateau current and a low onset potential. In our previous review, we argued that manipulations in nanostructures and doping strategies are necessary to increase the plateau current, while the surface properties of the semiconductor need to be improved to lower the onset potential [34]. In recent times, there has been many advancements in the nanostructure synthesis, bulk and surface modifications of hematite by forming heterostructures with various materials which overcome the obstacle of low minority carrier diffusion length and achieve improvements in photon absorption [24, 36, 38, 45]. Synthesis of different nanostructures (nanorods, dendritic nanowires, cauliflower-type, nanoflowers etc,) of hematite photoanodes have been reported by various groups [46–49].

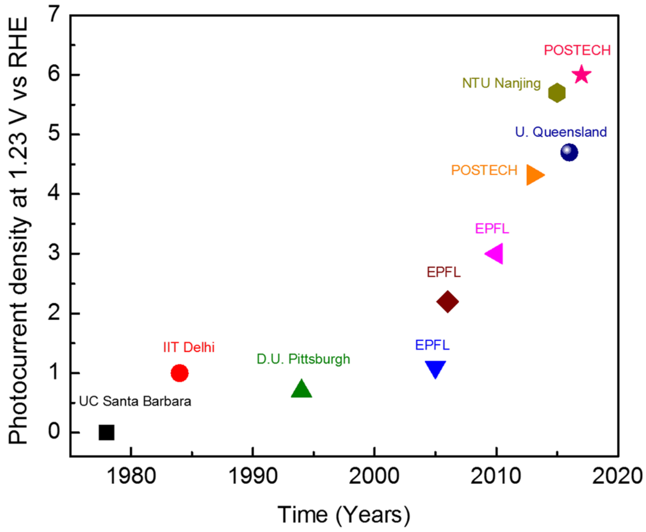

Figure 1. Progress in reported photocurrent density at 1.23 V versus RHE of hematite photoanodes with time in years [9, 30, 36–42].

2.1. Strategies to overcome bulk property limitations of hematite

The low inherent electrical conductivity of bulk hematite is one limitation that needs to be addressed [50, 51]. Undoped hematite has a very low electrical conductivity of 10^{-14} Ω^{-1} cm^{-1}, and electron mobility of 10^{-2} cm^2 V^{-1} s^{-1} [52–55]. These characteristics could be improved by adding suitable dopants to hematite. When tetravalent dopants, such as Ti, Zr, Sn, Mn, Ge and Si are added to replace some of the Fe^{3+} cations, the extra electrons donated to the crystal will increase its conducting electron concentration and retain its n-type conductivity [24, 47, 56–58]. When divalent dopants, such as Mg, Cu and Ni are added to replace Fe^{3+} cations in the crystal, hole carriers are created making the hematite p-type [59–61]. A list of dopants investigated in hematite and the resulting PEC performances are given in table 2. Elemental doping enhance the PEC performance of hematite by; (1) increasing the intrinsic conductivity, (2) generating a shallow donor level below the conduction band minima, which alter the absorption, (3) large cation substitution induces the strain within lattice and thus recombination centers. Fe^{3+} cation has an ionic radii of 55 pm and substituting a cation with larger ionic radii than 55 pm will create additional defects. In our previous study, Mn^{4+} cation were doped in hematite, which has similar ionic radius (53 pm) as Fe^{3+} (55 pm). Mn doping improves the PEC performance of hematite by increasing the carrier conductivity without creating the additional defects (similar UV–vis spectra with and without doping) and also enhance the OER kinetics at the electrode/electrolyte interface because of its good OER catalytic property [47].

One of the most commonly used dopants in hematite is Sn which has bigger ionic radii (69 pm) than Fe^{3+}. Annamalai and coworkers shows that Sn^{4+} doping improves the photocurrent of hematite and discussed that the Sn^{4+} doping induced a shallow donor level below the conduction band of hematite, which does not contribute to increase electrical conductivity because of its localized nature [62]. Additionally, Sn^{4+} introduction induce local micro-strain and a decreased Fe–O bond ordering. Sn^{4+} donor dopants in hematite lattices introduce electrons to Fe^{3+} sites and reduce to Fe^{2+}. These Fe^{2+} sites can thus improve the electrical conductivity of hematite photoanodes through the polaron hopping [62, 63]. Sn can be added intentionally. Alternatively, it could get introduced into hematite by diffusion from FTO glass which is frequently used as the conducting substrate in anodes, during its post annealing treatments [24, 56, 57, 64, 65]. In a study, it was shown that Sn^{4+} doping in a hematite nanorod anode improved its photoactivity, and its carrier concentration increased from 7×10^{19} to 2.45×10^{20} cm^{-3} [64]. Our group recently demonstrated a dual effect of Sn doping [24]. Sn doping was achieved by depositing a thin overlayer of SnO_x via atomic layer deposition (ALD) on FeOOH nanorods followed by annealing

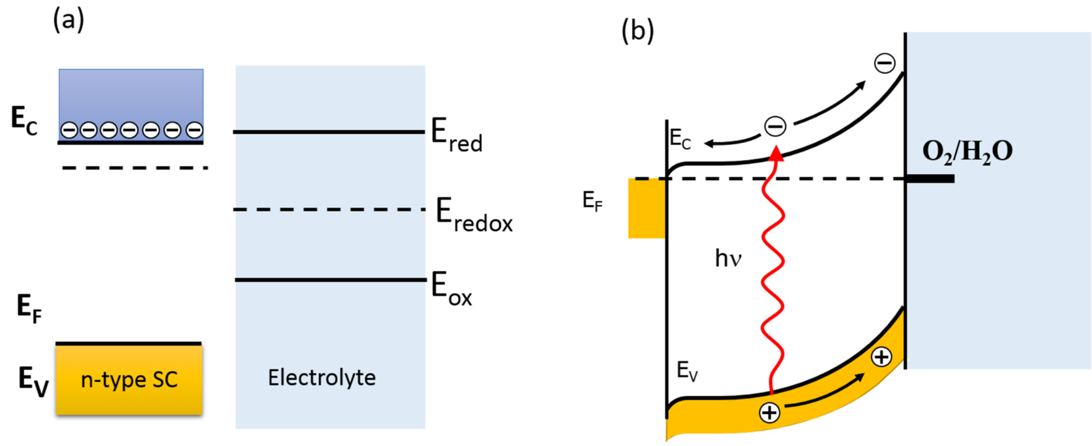

Figure 2. (a) The isolated energy band diagram of hematite and the electrolyte, (b) the equilibrated energy band diagram and the formation of space charge layer of hematite when it is immersed in to the electrolyte.

at 650 °C. This Sn doped hematite exhibited 3.1 mA cm^{-2} photocurrent density at 1.23 V versus RHE and also showed a cathodic shift in the onset potential when compared to the undoped hematite which was also annealed at 650 °C (figure 3). High annealing temperatures usually damage the FTO and increase its series resistance and hence, the lower annealing temperature used in this study was beneficial. The annealing temperature could be further reduced by employing two layers of SnO_2, an underlayer and an overlayer, to facilitate Sn diffusion from both sides during annealing [24, 66, 67].

Si^{4+} has also been shown as an effective dopant for hematite photoanodes. Gratzel *et al* reported Si doped, cauliflower structured hematite with a high donor density of 10^{20} cm^{-3}, which could enhance its PEC performance [68]. This cauliflower type, Si doped hematite photoanode exhibited a current density of 2.2 mA cm^{-2} at 1.23 V versus RHE. A large area (80 cm^2 active area), Si doped hematite synthesized by a dip coating method, exhibited ~1 mA cm^{-2} photocurrent density at 1.23 V versus RHE [69].

Ti is another element investigated for doping hematite [50, 56, 70–72]. In 1978, Kennedy *et al* reported that Ti doped hematite increased the carrier concentration to a level > 10^{19} cm^{-3} [40]. They also studied the effect of different electrolytes on the performance of hematite and found a higher photoconversion efficiency and a lower onset potential in 2 M NaOH (pH 13.8). Jiujun *et al*, also synthesized Ti doped hematite nanostructures by a hydrothermal method [56] which showed an urchin-like morphology, with enhanced effective surface area compared to undoped nanostructures. They obtained a remarkable plateau photocurrent density of 3.76 mA cm^{-2} for the Ti doped nanostructures under AM 1.5G in 1M NaOH electrolyte, which was 2.5 times higher than that obtained for undoped nanostructures (1.48 mA cm^{-2}) [56]. Recently Cho *et al* demonstrated a facile flame Ti doping method which reduced the onset potential (380 mV) and enhanced the PEC performance of hematite photoanodes [73]. This onset potential reduction is attributed to decreased bulk and surface recombination and a dense Fe_2O_3 under layer that reduced the back recombination. Oxalic acid and FeOOH surface treatment of Ti doped Fe_2O_3 helps to further improve the quality of electrode/electrolyte interface. Moreover, the Ti doped sample shows about two times higher photocurrent density of 1.58 mA cm^{-2} at 1.23 V RHE and 30% IPCE at 300 nm [73].

Even though it is not frequently reported, it is worth noting that another group IV element, Ge, has also been examined as dopant in hematite. A Ge-doped hematite film has been prepared by Liu *et al* using a hydrothermal approach with highly reactive Ge colloidal solutions used as dopant sources [74]. Ge-doped hematite nanosheet arrays showed a photocurrent density of 1.4 mA cm^{-2} at 1.23 V versus RHE, which was more than 50 times that of undoped hematite nanorod arrays. This improvement is thought to originate from the two orders of magnitude higher donor density of Ge-doped hematite than that of the undoped sample, which enhanced the electrical conductivity.

Platinum doping (combined with CoPi surface treatment) of hematite photoanode shows a stable performance of 4.32 mA cm^{-2} photo current at 1.23 V versus RHE under simulated 1 sun (100 mW cm^{-2}) [37]. The hematite nanorods were formed by annealing in two steps at 550 °C and 800 °C exhibited a unique ‘wormlike’ morphology. Platinum doping improved the electrical conductivity of hematite by increasing its donor density to 3.27×10^{17} cm^{-3}, 2.77×10^{18} cm^{-3}, and 3.91×10^{18} cm^{-3} for pure Fe_2O_3, Pt doped Fe_2O_3, and Pt doped Fe_2O_3/CoPi, respectively [37].

Ru doped nanoporous hematite nanorod photoanode was reported by Xueli *et al* which was synthesized via a doctor blade method followed by 700 °C annealing at ambient atmosphere [36]. The optimized Ru doped hematite photoanode displayed a record photocurrent density of 5.7 mA cm^{-2} 1.23 V versus RHE and an onset potential of 0.7 V versus RHE. This excellent PEC performance is probably due to the enhanced charge carrier concentration and mobility [36].

To summarize, introducing optimum doping concentrations has been shown to be beneficial for altering the inherent electronic properties of hematite, which in turn enhances the plateau photocurrent of PEC cells. It should be emphasized that the actual effectiveness of any of these intentional elemental dopants is sometimes difficult to isolate because of the effects of contaminant Sn, which unintentionally diffuses from

Table 2. Hematite photoanodes doped with different elements and their PEC performance.

Dopant	Photocurrent density (mA cm^{-2})	Potential versus RHE	IPCE @ 1.23 V versus RHE	Electrolyte	Dopant concentration ($10^{19} \times$ cm^{-3})	Surface morphology	Ref.
Mn	1.60	1.23	23% @ 350 nm	1M NaOH	3.0	Nanorods	[47]
Sn	1.86	1.23	19% @ 370 nm	1M NaOH	5.38	Nanowire	[65]
Sn	2.10	1.60	24% @ 350 nm, and 1.4 V	1M NaOH	114.0	Nanoflakes	[75]
Sn	2.80	1.24	68% @ 350 nm	1M NaOH	N/A	Nanorods	[73]
Sn	2.70	1.23	27% @ 350 nm	1M NaOH	0.17	Nanocrystal	[81]
Sn	3.10	1.23	70% @ 350 nm	1M NaOH	11.8	Nanorods	[24]
Si	2.30	1.40	39% @ 350 nm, and 1.4 V	1M NaOH	N/A	Nanostructure	[39]
Si	0.72	1.23	14% @ 350 nm	1M NaOH	N/A	Thin film	[69]
Si	2.20	1.23	45% @ 350 nm	1M NaOH	N/A	Nanocrystal	[82]
Si	1.45	1.23	Not available	1M NaOH	N/A	Nanocrystal	[39]
Si	4.00	1.53	Not provided	1M NaOH	20.0	Cauliflower	[46]
Pt	1.43	1.42	65% @ 350 nm	1M NaOH	0.27	Wormlike	[37]
Sn/In	2.50	1.23	Not provided	1M NaOH	N/A	Thin film	[83]
Ti	2.44	1.23	48% @ 350 nm	1M NaOH	1.49	Nanorods	[83]
Ti	2.28	1.23	27% @ 350 nm	1M NaOH	N/A	Nanostructure	[70]
Ti	1.91	1.23	62% @ 350 nm	1M NaOH	1.36	Thin film	[56]
Ti	1.83	1.02	24% @ 350 nm	1M NaOH	N/A	Thin film	[67]
Ti	1.58	1.23	29% @ 350 nm	1M NaOH	N/A	Nanorods	[73]
Ti	1.86	1.43	47% @ 350 nm and 1.43 V	1M NaOH	N/A	Nanoporous	[84]
Ti	2.50	1.23	55% @ 350 nm	1M NaOH	67.9	Dendritic nanowires	[48]
Zr	2.10	1.66	Not provided	1M NaOH	260	Thin film	[57]
Mo	1.50	1.32	8% @ 350 nm	1M NaOH	N/A	Spindle	[85]
Al	1.10	1.32	5.2% @ 350 nm	1M NaOH	147	Thin film	[86]
Nb	0.65	1.56	19% @ 350 nm	1M NaOH	N/A	Ultrathin film	[87]
Ta	0.45	1.6	30% @ 350 nm	0.5 M Na_2SO_4	N/A	Thin film	[88]
Cu	0.07	1.66	Not provided	1M NaOH	N/A	Thin Film	[60]
Cr	0.70	1.32	5% @ 350 nm	1M NaOH	N/A	Nanorods	[89]
Ni	1.50	1.67	36% @ 350 nm	1M NaOH	23.9	Nanotubes	[61]
Mg	0.45	1.23	Not provided	1M NaOH	N/A	Nanoparticles	[59]
P	2.70	1.23	Not provided	1M NaOH	10.1	Nanowires	[90]
Ru	5.70	1.23	82% @ 320 nm	1M NaOH	97.0	Nanorods	[36]

FTO substrates during the high temperature, post annealing (750 °C–800 °C) of hematite [24, 63, 65, 75]. In addition to the issue of low carrier concentration, one needs to address the interfacial reaction limitation of hematite photoanodes also to improve the photoanode performance. Surface treatment with co-catalysts or depositing surface passivation layers are possible approaches to reduce the charge recombination at electrode/electrolyte interface. This will be discussed in the next section [76–80].

2.2. Strategies to overcome the surface property limitations of hematite

An additional shortcoming of hematite photoanode is the need for an overpotential which is attributed to the sluggish hole transport across the semiconductor/electrolyte interface [78, 91–93]. The overpotential required for hematite can be reduced either by lowering the potential-dependent rate constant for surface-mediated charge recombination, or by increasing the rate constant for hole transfer from the photoelectrode to the molecular reactant [73, 77, 94]. The former can be accomplished by passivating the localized electron trap states on the surface, e.g. by deposition of overlayers or by chemical treatments [76, 91]. The rate constant for hole transfer across the interface could be improved by deposition of an OER catalysts. In this section we will discuss the recent attempts reported to lower the overpotential of hematite photoanodes for PEC water oxidation [80, 94].

OER catalysts loaded on the surface of hematite facilitate water oxidation reactions usually through the oxidation of the metallic element of the catalyst, which inject holes from the hematite surface into the electrolyte [78, 95]. Various OER catalysts like CoPi [94, 96], IrO_2 [42, 78], CoO_x [44, 97], MnO [95] and FeNiOx [80, 98] have been extensively studied on hematite photoanodes (table 3). Nocera *et al* developed the CoPi OER catalyst, which they integrated with various photoanodes, including hematite, as a cocatalyst [96, 99], and studied its working mechanism by XANES and EPR techniques. They concluded that the metallic element Co in CoPi oxidized from Co(II) to Co(III) and Co(IV), leading to the formation of high-valence Co(IV)–O intermediates [100, 101]. Since the development of CoPi, it has gained a lot of acceptance because of its low overpotential of only 0.41 V required to oxidize water at pH 7 [102]. IrO_2 is a well-known OER catalyst

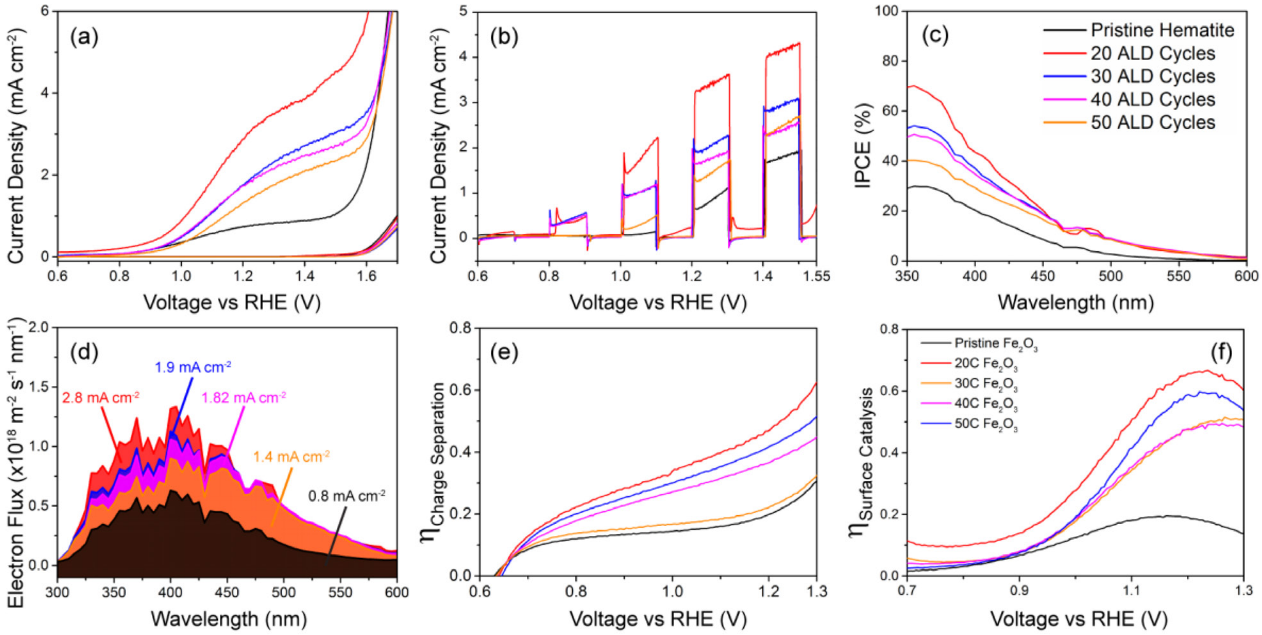

Figure 3. PEC experimental data obtained in undoped hematite anode and SnO_x coated hematite anodes at 20–50 ALD cycles measured under AM 1.5G 100 mW cm^{-2} in 1M NaOH electrolyte solution. (a) Photocurrent-potential curve, (b) chopped photocurrent-potential curve, (c) IPCE action spectrum collected at 1.23 V versus RHE, (d) electron flux and calculated integrated photocurrent based on IPCE data previously shown, (e) charge separation efficiency for water oxidation and (f) surface catalysis efficiency for water oxidation. [24] John Wiley & Sons. © 2017 Wiley-VCH Verlag GmbH & Co. KGaA, Weinheim.

Table 3. Hematite photoanode with various surface passivation layers and cocatalysts for water oxidation.

Surface overlayer/cocatalyst	Photocurrent density (mA cm^{-2})	Potential versus RHE	Cathodic shift in onset potential (mV)	Electrolyte	References
Al_2O_3	2.30	1.23	100	1M NaOH	[76]
TiO_2	1.20	1.23	190	1M NaOH	[77]
TiO_2	1.90	1.23	110	1M NaOH	[108]
TiO_2	1.01	1,23	100	1M NaOH	[110]
SnO_x	2.25	1.23	62	1M NaOH	[64]
SnO_x	3.12	1.23	100	1M NaOH	[24]
SiO_x	2.44	1.23	90	1M NaOH	[111]
ZnO	1.08	1.23	170	1M NaOH	[112]
Ga_2O_3	0.25	1.02	200	1M NaOH	[91]
In_2O_3	0.15	1.02	130	1M NaOH	[91]
Co_3O_4	1.20	1.23	40	1M NaOH	[97]
Co_3O_4	1.48	1.23	60	1M NaOH	[113]
CoO_x	0.45	1.23	100	0.1M NaOH	[92]
CoF_3	0.15	1.00	200	1M NaOH	[114]
CoPi	0.30	1.23	230	0.1M KPi	[115]
CoPi	1.20	1.23	200	1M NaOH	[99]
CoPi	2.80	1.23	170	1M NaOH	[79]
IrO_2	3.00	1.23	200	1M NaOH	[42]
$Ni(OH)_2/IrO_2$	1.60	1.23	200	1M NaOH	[78]
$FeNiO_x$	2.75	1.23	200	1M KOH	[80]
$Ni_xFe_{2-x}O_3$	1.00	1.23	60	1M KOH	[61]
$NiFeO_x$	1.20	1.23	550	0.5M KPi	[93]
NiFe	2.10	1.23	300	1M NaOH	[98]
FeOOH	1.21	1.23	120	1M NaOH	[116]
$Ni(OH)_2$	0.40	1.23	300	1M KOH	[117]
Ni–Bi	0.60	1.23	200	1M NaOH	[118]

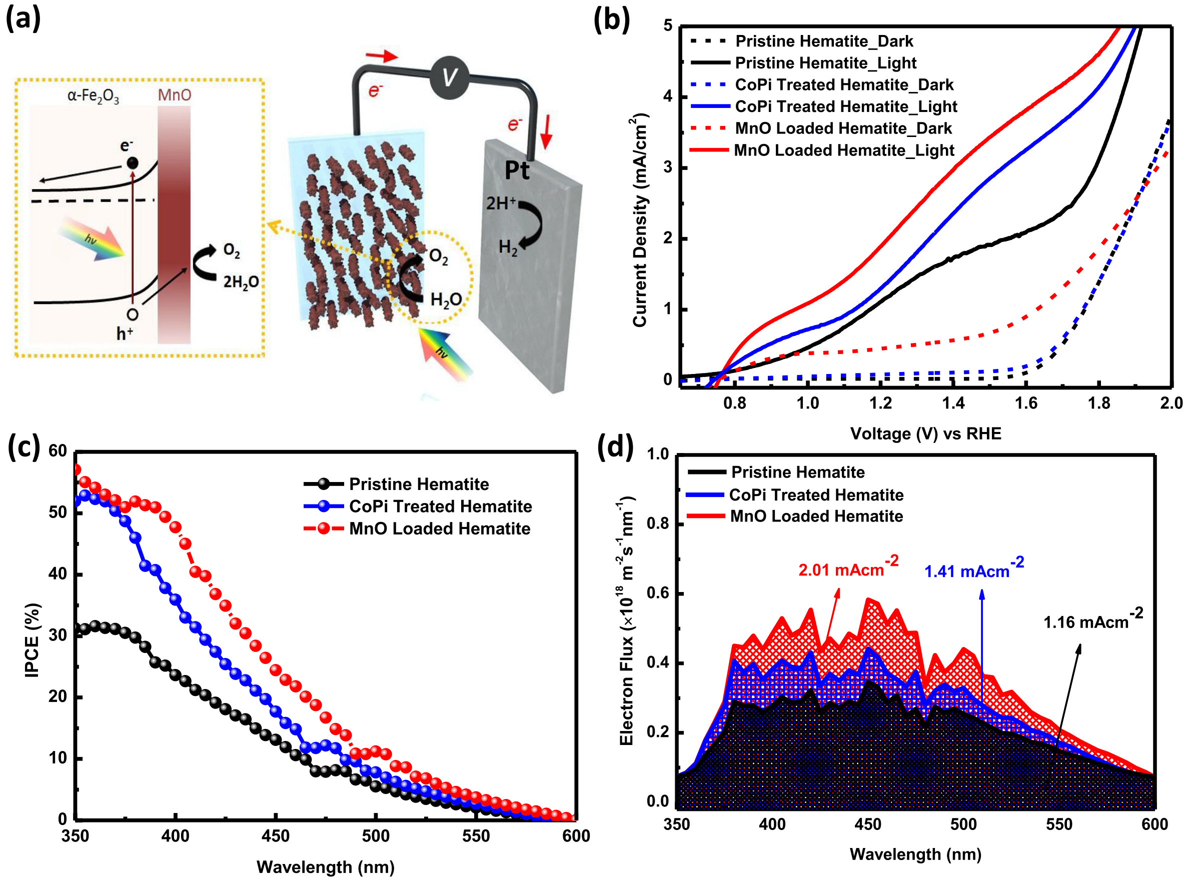

Figure 4. (a) Schematics of MnO loaded hematite photoanode, (b) photocurrent-potential curve of pristine hematite photoanode MnO loaded hematite and CoPi treated hematite measure under AM 1.5G 100 mWcm^{-2} in 1M NaOH electrolyte solution, (c) IPCE action spectrum of pristine hematite, MnO loaded hematite, and CoPi treated hematite collected at 1.23 V versus RHE and (d) photon and electron flux observed from pristine, MnO loaded hematite and CoPi treated hematite samples. [95] John Wiley & Sons. © 2016 WILEY-VCH Verlag GmbH & Co. KGaA, Weinheim.

which shows lower over potentials of 250 mV and 300 mV in alkaline and neutral pH conditions respectively for water oxidation [103, 104]. Tilley *et al* demonstrated that an IrO_2 nanoparticle coated hematite photoanode could generate an excellent photocurrent density of 3.0 mA cm^{-2} at 1.23 V versus RHE and a 200 mV reduction in overpotential [42]. IrO_2 nanoparticles on the surface of hematite catalyzed the transfer of photogenerated holes resulting in lowering of the required overpotential while a higher photocurrent was achieved by nanostructuring of the hematite which ensured lower charge carrier recombination.

Recently, $FeNiO_x$ OER catalyst is extensively used because of its earth abundance, high stability in alkaline solution and easy integration with any photoanode [105–107]. Xile Hu's group integrated $FeNiO_x$ cocatalyst with cauliflower type hematite via PEC deposition. This $FeNiO_x$-coated nano Fe_2O_3 sample shows ~250 mV and 100 mV cathodic shifts in onset potential as compared to bare hematite and CoPi treated hematite photoanodes, respectively [80]. Dunwei Wang's group also reported similar $FeNiO_x$ coated hematite with an impressive cathodic shift of ~550 mV in onset potential where a simple regrowth mechanism has been used to synthesize the hematite photoanode, and $FeNiO_x$ cocatayst was deposited subsequently by a drop casting method [93]. Recently, our group demonstrated that an ultrathin MnO could be an effective cocatalyst with hematite anode for OER [95]. Ultrathin MnO nanoparticles integrated with hematite photoanode exhibits a ~200 mV cathodic potential shift and improved PEC performance, which is comparable to CoPi (figure 4). The detail findings of this study will be discussed in the next section [95].

Another common strategy to overcome the sluggish hole injection from hematite surface to electrolyte is to reduce the surface recombination rate by using thin overlayers of wide band gap metal oxides. A few surface passivation strategies such as TiO_2 [77], Al_2O_3 [76], Ga_2O_3 [91], and SnO_x [24] have been reported so far.

Recently, Wonyong Choi's group reported good stability for over 100 h in a hematite photoanode with photocurrent density of 6 mA cm^{-2} at 1.23 V versus RHE under 1 sun illumination [30]. This excellent performance of hematite nanorod photoanode could be attributed to the combined effects of H_2 treatment, TiO_2 and CoPi overlayers. Hydrogen treatment enhances the electrical conductivity, ultrathin TiO_2 overlayer reduces the surface charge recombination, and CoPi enhances the rate of reaction at the electrode-electrolyte interface [30]. Mahmoud *et al* also studied a simple solution grown TiO_2 as a surface passivation layer on nanostructured hematite

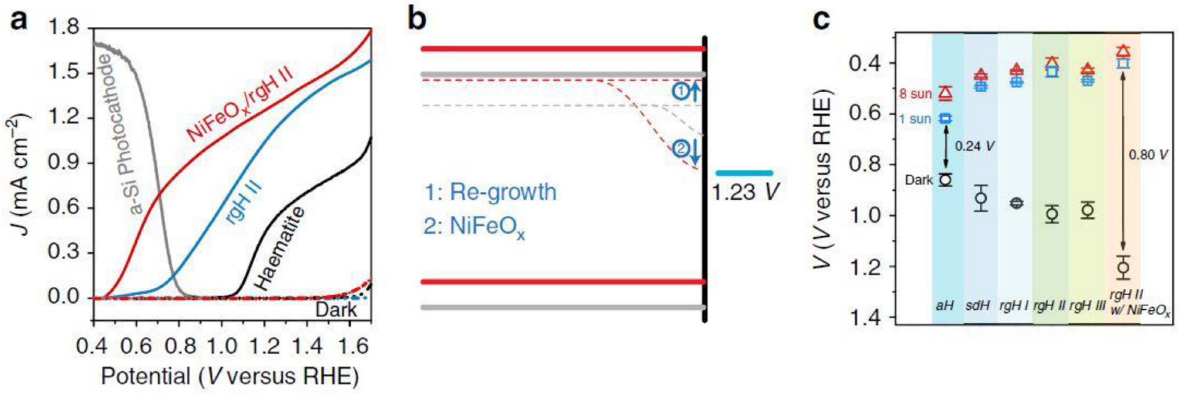

Figure 5. (a) Photocurrent-potential curves of as grown hematite, regrowth treated (rgh) hematite and $NiFeO_x$ coated rgh hematite photoanodes measure under AM 1.5G 100 mW cm^{-2} in 1M NaOH. (b) Band diagram of unmodified hematite (grey) and $NiFeO_x$-decorated hematite after re-growth treatments (red) under flat-band, quasi-equilibrium conditions. and (c) open circuit potential measurements of various hematite photoanodes under 8-sun (red, triangle), 1-sun (blue, square) and dark (black, circle) conditions. Reproduced from [93].

surface and showed a cathodic shift of 190 mV in onset potential and 4.5 times improvement in photocurrent density [77]. Our group showed that an ultrathin TiO_2 layer deposited on hematite nanorods by ALD exhibits 1.9 mA cm^{-2} photocurrent at 1.23 V and ~200 mV cathodic shift in onset potential [108]. More recently, Piangjai *et al* discussed the combined effect of plasmonic Ag nanoparticles and CoPi catalyst with hematite photoanode [38]. This Ag and CoPi nanoparticles modified hematite showed an excellent photocurrent density of 4.68 mAcm^{-2} at 1.23 V versus RHE which is attributed to the presence of plasmonic Ag nanoparticles which improved light harvesting and facilitated charge transfer while Co–Pi works as a cocatalyst for water oxidation and helps to reduce the surface recombination [38].

We demonstrated that the recombination sites on hematite surface can be reduced by passivating the nanorods with another layer of hematite [109]. A core–shell type architecture of hematite nanorod photoanode was produced where a thin hematite shell was sprayed on hematite nanorods which has proven to partially passivate these surface effects. Dunwei Wang's group also reported similar effect by regrowth of a thin FeOOH layer over hematite followed by annealing [93]. This regrowth strategy resolves the near surface disorder and hence improves the photovoltage generated by hematite (figure 5) [93].

2.3. Surface charge transfer mechanism of hematite

As discussed in section 2.2, the sluggish hole transfer from the electrode to electrolyte at the interface can be enhanced by employing cocatalysts or by noncatalytic passivation layers. These two techniques are now understood to have fundamentally different operating mechanisms in assisting the hole transport. Surface passivation (a non-catalytic process) implies the reduction of hematite surface defects which reduces the hole–electron recombination rate, while a cocatalyst usually implies the oxidation of the metallic element of the cocatalyst which enhances the rate of hole transfer from the hematite surface to the electrolyte [43, 95, 119].

Many attempts have been made to shed the light on the operating charge transfer mechanisms through systematic studies using intensity-modulated photocurrent spectroscopy (IMPS) [43, 95, 120]. IMPS allows the charge carrier dynamics at the electrode/electrolyte interface to be de-convoluted into contributions from charge transfer and surface recombination. It is an attractive technique for understanding the surface carrier dynamics at the semiconductor/electrolyte interface. In our previous study, we reported the surface effects of manganese (Mn) doping, and of a thin passivation (shell) layer of highly crystalline Fe_2O_3 on hydrothermally grown hematite nanorods [121]. Our study revealed that although the photocurrent enhancements achieved by both modifications are similar, the operating mechanisms are fundamentally different. Mn doped hematite shows an enhancement in PEC performance due to increase in hole transfer constant, while the core–shell hematite shows a decrease in charge recombination rate constant (figure 6) [121].

This observation indicates that the core–shell architecture is effective in improving the photocurrent by suppressing surface recombination, rather than by increasing charge transfer. The finding that Mn doping improves the surface hole transfer kinetics was rather unexpected but a similar observation has been reported in Sn-doped hematite by Dunn *et al* [120] who demonstrated that Sn-enrichment at the surface improved the catalytic properties at the surface (figure 7).

We have also shown by IMPS in an ultrathin MnO nanocrystals decorated hematite and CoPi treated hematite (figure 8) that the MnO loaded hematite sample shows an increased hole transfer rate constant compared to bare hematite. The CoPi treated hematite, on the other hand, shows a decrease in charge recombination rate, while hole transfer rate was similar to that in bare hematite [95]. Peter *et al* also reported a similar observation on Sn doped hematite [120]. The increased transfer efficiency brought about by Sn-doping hematite was attributed to enhanced catalysis of the OER rather than to surface passivation. While it may not be clear at present how the Sn dopant beneficially impacts on the OER kinetics, the insight that dopants can speed up the sluggish

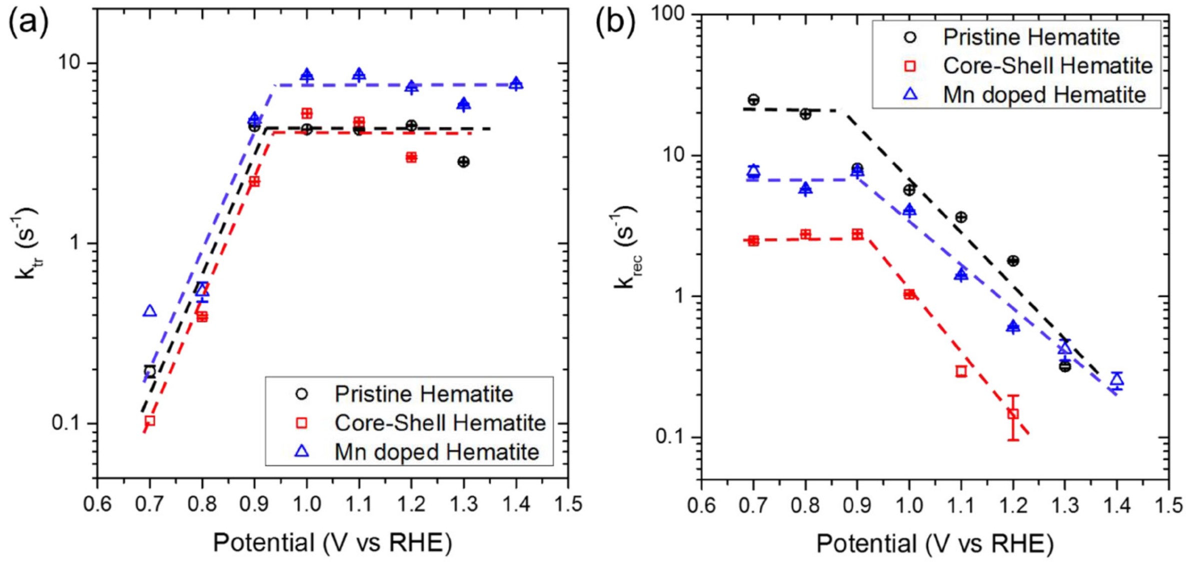

Figure 6. (a) Charge transfer rate constant ktr and (b) surface recombination rate constant krec of pristine, Mn-doped and core–shell hematite samples as a function of potential. Reprinted with permission from [121]. Copyright 2017 American Chemical Society.

OER is an important milestone in the optimization of photoanodes for water oxidation [120]. Dunwei Wang's group also studied $NiFeO_x$ coated hematite photoanode by IMPS technique [122]. They showed that the best performing hematite, in terms of photocurrent onset potential, exhibited the slowest water oxidation rate constants. When amorphous $NiFeO_x$, a water oxidation catalyst, was present, the rate of surface holes transfer actually slowed down; resulting in low recombination rate at the hematite surface (figure 9). They concluded that the $NiFeO_x$ primarily serves as a passivation layer rather than a catalytic layer [122].

Finally, the need for overpotential in water splitting is attributed to two causes: (i) the position of the valance band of hematite, which is 0.4–0.5 V too positive to allow water splitting and, (ii) the sluggish hole transport at the semiconductor/water interface. This opens a new direction of search for a better, alternative iron-based material for highly efficient water splitting which must be robust, stable and must have good carrier conductivity. More importantly, its energy band gap should not be more than 2.2 eV because it limits the maximum STH conversion efficiency.

3. Fe_2TiO_5 as a photoanode material

In previous sections, we discussed the strategies employed to improve Fe_2O_3 based PEC devices by doping and by surface treatments with thin overlayers and cocatalysts. However, these actions do not address the underlying limitations of hematite namely small minority carrier diffusion length and poor charge transport properties. Although, these limitations have been mitigated somewhat by nanostructuring to increase the space charge layer; surface charge transfer kinetics and poor OER of hematite are still significant impediments for the realization of commercial PEC cells. This makes it inevitable that we explore new systems with better charge transport properties, longer diffusion length of minority carriers and improved surface reaction kinetics. It has been noted that some complex metal oxides may have desirable properties for consideration as an alternative to hematite. A report on such complex metal oxides has been recently compiled by Abdi *et al* which uncovers a range of materials and their development for application in solar water splitting [123]. One way to improve the intrinsic properties of Fe_2O_3 is to amalgamate with another material, such as TiO_2, which inherently has good carrier conductivity and large charge diffusion length. A scrutiny of the Fe–Ti–O ternary system might give indications for an alternative material with the best combination of the desired properties of both Fe_2O_3 and TiO_2. This is corroborated by the evidence that Ti is an effective dopant to tune the band level positioning in Fe_2O_3. When exploring a novel material for photoabsorber, it is imperative to understand both its bulk and surface characteristics. Surface characteristics are often correlated with the morphology of films and post deposition treatments, but bulk characteristics depend on the intrinsic electron band and crystal structures.

One candidate material in the Fe–Ti–O ternary system that has received considerable attention in recent times is Fe_2TiO_5 pseudobrookite which possesses an orthorhombic structure with a Cmmm space group [124]. The cations in the Fe_2TiO_5 crystal are located in two different octahedral sites M1 and M2 but the actual distribution of Fe^{3+} and Ti^{4+} ions in these sites has not been conclusively determined. Fe_2TiO_5 comprises abundant and non-toxic elements and can be produced simply by the oxidation of ilmenite ore at temperatures above 1000 °C with rutile as the byproduct [125]. In the form of a film, it has a good thermodynamic and aqueous stability in a wide pH range. These properties make it a potential candidate as a photocatalyst for solar water splitting.

Some early reports on Fe_2TiO_5 have been on its crystal growth and its characterization [127–129]. It is an n-type semiconductor with band gap of around 1.9–2.1 eV which covers a large part of solar spectrum. In a recent report, Guillaume *et al* presented a crystal structural analysis for Fe_2TiO_5 pseudobrookite composition (shown in figure 10(a)) [126]. Through various coupled techniques like ^{57}Fe Mössbauer spectroscopy, XRD etc, they deduced that the optical properties and the phase purity strongly depend on the thermal history and the chemical composition which influences the cationic vacancy concentration. It was also noted that obtaining the pure phase Fe_2TiO_5 by solid state reaction route is very challenging because a hematite-rich phase is usually obtained in this synthesis. This issue has been tackled by adding an excessive amount of titania to the desired Fe_2TiO_5 stoichiometry (i.e. $Fe^{+3}/Ti^{+4} < 2$) in the starting reactants.

There have been reports on the dielectric properties and electrical conductivity of Fe_2TiO_5 bulk samples [130–132]. Sharma *et al* investigated the complex dielectric and impedance properties of Fe_2TiO_5 and reported that its non-Debye type dielectric relaxation follows a thermally activated process [131]. This was attributed to the polaron hopping type conductivity mechanism which was confirmed by AC conductivity analysis. Nikolic *et al* reported changes in electrical conductivity in accordance with Jonscher's power law for nanopowder and bulk samples [130]. They also concluded that the quantum mechanical-tunneling model for the case of small polaron hopping can be applied at higher temperatures which outlines the conductivity in Fe_2TiO_5.

The pseudobrookite, Fe_2TiO_5 phase has exhibited diverse characteristics like the gas sensing ability, magnetic properties and photocatalytic properties which have been exploited previously for various applications [133–138]. Very recently, a novel yellow pigment, Fe_2TiO_5 decorated mica composites was evaluated for its near infrared reflectance ability which makes it a good candidate as solar reflective coating [139]. The near infrared solar reflectance of this composite was demonstrated to be as high as 80.3% which could reduce the interior temperature in a building by about 3 °C. This characteristic could be utilized for thermal insulation of solar devices also in the large scale.

Many researchers have reported synthesis of nano and micro particles of Fe_2TiO_5 and examined their potential in a variety of applications. Growth of nanocrystalline Fe_2TiO_5 perovskite thin films assisted by microwave irradiation was studied by Phani *et al* [140] while the synthesis of Fe_2TiO_5 nanoparticles was reported by Min *et al* who considered them for Li-ion electroactivity [141]. Synthesis of porous microparticulates of Fe_2TiO_5 has been explored by Guo *et al* for its electrochemical activity as anode material [142]. Ku *et al* used Fe_2TiO_5 as an oxygen carrier for chemical looping process. Its high equilibrium constants resulted in high syngas conversion in the fixed bed reactor [143].

An efficient photoanode must absorb a significant amount of visible light. The energy band gap of a material indicates the range of the wavelengths that could be absorbed from the solar spectrum, but it is the absorption coefficient that signifies the actual number of photons absorbed. The absorption coefficient of Fe_2TiO_5 is found to be around 4.6×10^4 cm^{-1} at a wavelength of 500 nm which translates into a required thickness of 650 nm to absorb 95% of incident light ($=3/\alpha$ where α is absorption coefficient). This implies that the photoelectrode film should be about 650 nm thick to absorb most of the photons at 500 nm wavelength. This makes Fe_2TiO_5 thin films vulnerable for insufficient photon absorption in compact or thin film forms. The important properties such as conductivity, mobility and carrier lifetime for Fe_2TiO_5 have been largely unexplored. Since these properties contribute to the charge transport in bulk and significantly impact on their performance in PEC cell, it would be important to characterize them carefully.

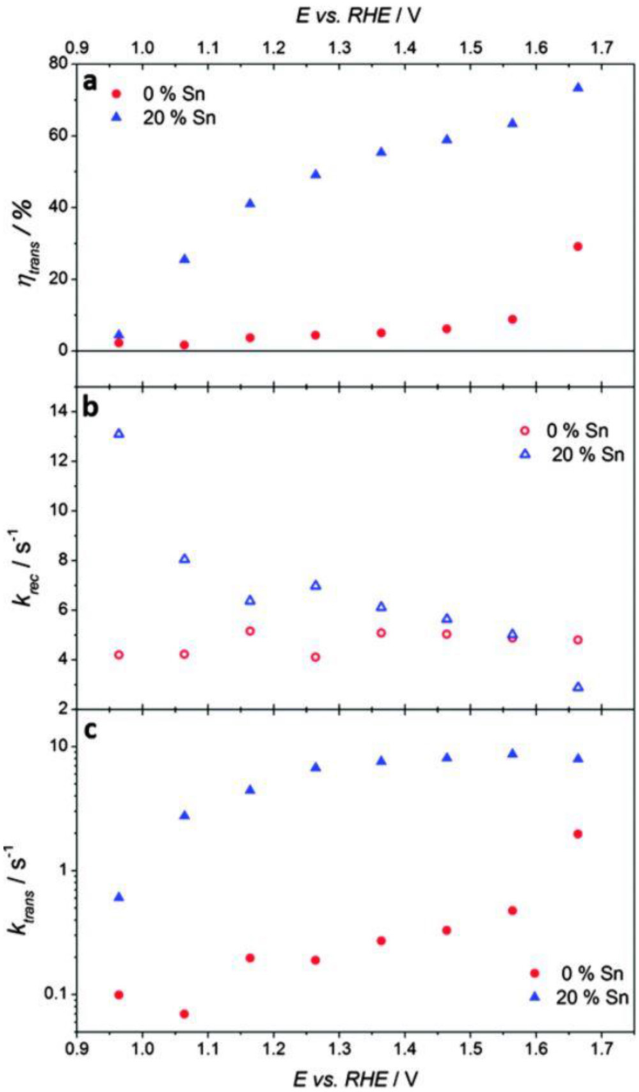

Figure 7. Parameters extracted from IMPS of photoanodes prepared with 0% and 20% Sn-precursor in the synthesis, illuminated by a 470 nm LED, intensity 10^{17} cm^{-2} s^{-1}. (a) Transfer efficiency, (b) rate constant for electron–hole recombination, (c) rate constant for hole transfer. Reproduced from [120].

We demonstrated the synthesis of pure phase Fe_2TiO_5 by a solvothermal technique, using isopropanol as the solvent for the precursors [25]. Nanoporous thin films were synthesized on FTO substrates by this technique and coated with a SnO_x overlayer for surface passivation to investigate its PEC performance. It yielded a photocurrent density of 0.35 mA cm^{-2} at 1.23 V versus RHE under 1 sun irradiation. Ultraviolet

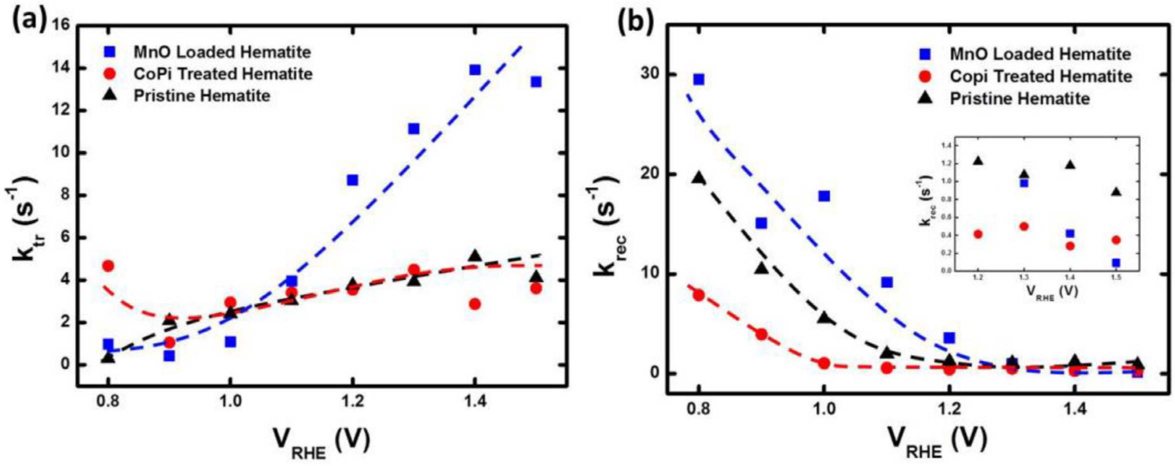

Figure 8. (a) Charge transfer rate constant (ktr) of as-prepared, CoPi treated, and MnO loaded hematite samples as a function of potential. (b) Charge recombination rate constant (krec) of as-prepared, CoPi treated, and MnO loaded hematite samples as a function of potential. The inset shows the magnification of krec at potentials larger than 1.2 V versus RHE. [95] John Wiley & Sons. © 2016 WILEY-VCH Verlag GmbH & Co. KGaA, Weinheim.

photoelectron spectroscopy (UPS) measurements showed that its band levels straddle the water redox levels with a work function of around 4.77 eV (figure 10(b)). This was later confirmed by Deng *et al* who reported a similar valence band of around −6.31 eV for a Fe_2TiO_5 layer synthesized by Ti treatment of a hematite layer [144].

Although we confirmed that our layer consisted pure phase of Fe_2TiO_5, the photocurrent density was still lower than those we obtained in Fe_2O_3 based films which were of the order of 1 mA cm^{-2}. This is attributed to the low Fe_2TiO_5 film thickness of 150 nm used which is insufficient for significant photon absorption. To realize the full potential of Fe_2TiO_5, it is necessary to improve its quantum efficiency. Recently, An *et al* reported inverse opal Fe_2TiO_5 prepared using polystyrene (PS) photonic crystals as templates [145]. Since a photonic crystal confines photons and allows coherent multiple scattering, it can potentially increase the overall absorption compared to a thin film. The performance of a Fe_2TiO_5 photonic crystal synthesized from 250 nm PS spheres (measured using 250 mW cm^{-2} light source) showed higher photocurrent density when compared to the disordered sample. Therefore, photonic crystal certainly improved absorption which could be beneficial, in general, for other Fe_2TiO_5 based PEC systems.

Very recently, Zhang *et al* used an iron titanate nanotube array with a TiO_2 underlayer, and modified it by hydrogen treatment and $FeNiO_x$ cocatalyst to improve its PEC activity [146]. The nanotube photoanode achieved a photocurrent density of 0.93 mA cm^{-2} at 1.23 V_{RHE} under 1 sun (100 mW cm^{-2}) irradiation with a cathodic shift in photocurrent onset potential of ~280 mV relative to the pristine nanotube array electrode (figure 11). This is one of the highest performances achieved for a modified iron titanate based photoanode under standard conditions. The reports enumerated above catapulted the research activity on Fe_2TiO_5, especially on Fe_2O_3/Fe_2TiO_5 heterojunctions and were later modified/integrated with other layers to realize higher performance PEC cells which would be discussed in the next section.

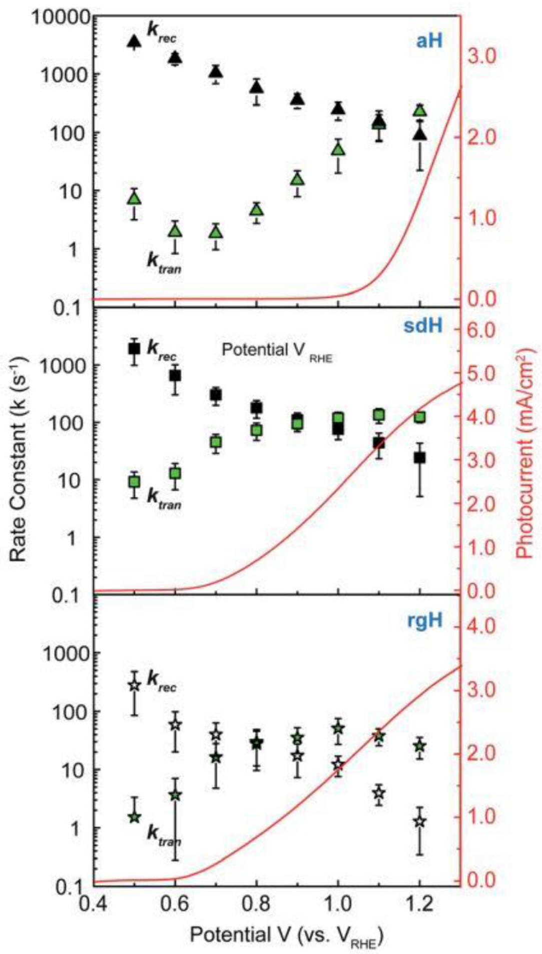

Figure 9. Rate constants extracted from IMPS data at different applied potentials. Rate constants of recombination are shown as black symbols; rate constants for surface charge transfer are shown as green symbols. The error bar is the standard deviation between different samples (typically 4–5 samples are measured for each group of data). Acronyms aH, sdH and rgH denote atomic layer deposited, solution grown and regrowth treated hematite respectively. Reproduced from [122]. CC BY 3.0.

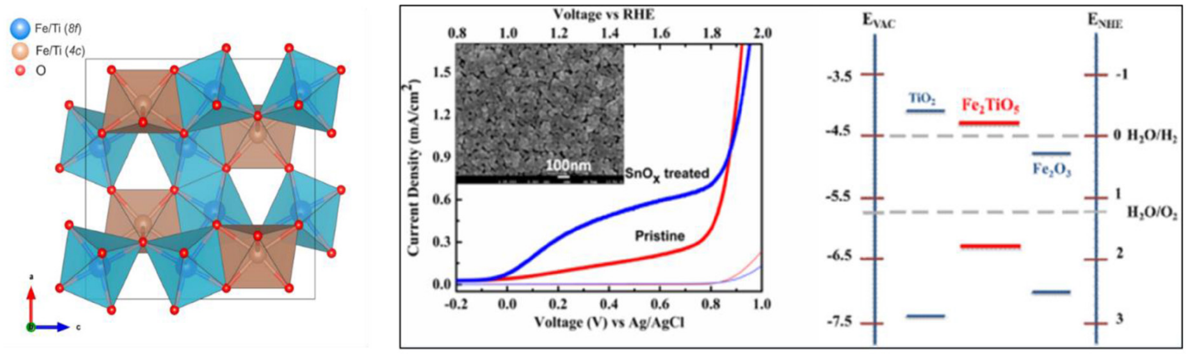

(a) (b)

Figure 10. (a) Representation of Fe and Ti sites in pseudobrookite structure. Reprinted with permission from [126]. Copyright © 2016, American Chemical Society, and (b) JV plots along with probable band level positions for Fe_2TiO_5 films calculated using ultraviolet photoelectron spectroscopy. Reprinted with permission from [25]. Copyright © 2014 American Chemical Society.

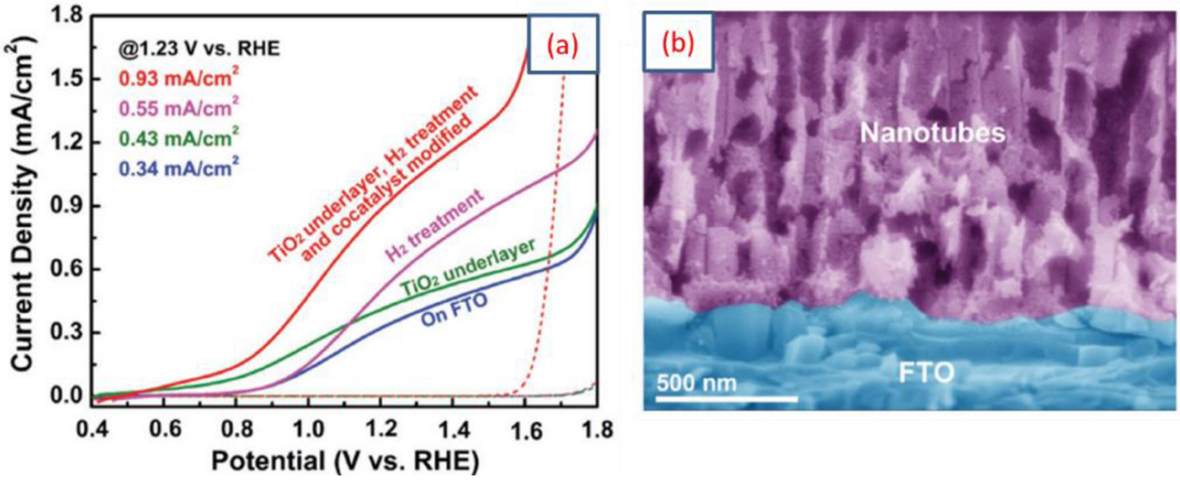

Figure 11. (a) *J–V* plots for Fe_2TiO_5 nanotube array on FTO modified with TiO_2 underlayer, H_2 treatment, and cocatalyst modification along with their respective control sample and (b) synthesized Fe_2TiO_5 nanotubes on FTO substrate. [146] John Wiley & Sons. © 2017 WILEY-VCH Verlag GmbH & Co. KGaA, Weinheim.

4. Iron oxide based heterostructures

In the last decade, hematite has been used comprehensively in heterostructures with various photoanodes. Shen *et al* has reviewed the charge carrier dynamics and material design of such heterojunctions in detail [147]. In the last three years, many reports, specifically on integrating Fe_2O_3 with Fe_2TiO_5 layers and with other iron based metal oxides, have emerged. Such integrated systems have proven to be effective in tackling both bulk and surface issues related to recombination along with the slow kinetics of water oxidation. In the following section, the Fe_2O_3/Fe_2TiO_5 heterojunction systems are discussed specifically.

4.1. Fe_2O_3/Fe_2TiO_5 heterojunctions

In the last section, we focussed the discussion on developments in pristine Fe_2TiO_5 as a photocatalyst or photoanode but it is worth highlighting that the photocurrent density reported is still lower than those obtained in pristine hematite based systems. This could be primarily due to the early, exploratory nature of the investigation into these novel material; optimization of its annealing processes, film morphology and defect densities etc are yet to be achieved. In addition, Fe_2TiO_5 possesses lower absorption coefficient requiring thicker films to absorb a significant amount of photons which implies that charge separation could become an issue even if significant number of photons are absorbed. Despite the low absorption coefficient, Fe_2TiO_5 may still perform better than TiO_2 due to its lower band gap which could absorb a larger wavelength proportion of the sun light. One of the early state-of-the-art TiO_2/Fe_2TiO_5 heterojunction based PEC device was developed by Liu *et al* where they obtained a remarkable photocurrent density of around 4.1 mA cm^{-2} at 1.23 V versus RHE with low onset potential of 0.2V [148]. The theoretical maximum photocurrent of TiO_2 itself is only around 2 mA cm^{-2} based on its bandgap [149]. This means the additional photocurrent in this heterojunction is contributed by Fe_2TiO_5. This study attributes the enhanced photocurrent density to the good band alignment with TiO_2 (as shown in figure 12(a)) and CoO_x which was used as an electrocatalyst. In this structure, Fe_2TiO_5 acted as an ultrathin absorber layer for TiO_2 nanotubes which complemented narrow absorption range of TiO_2 nanotubes,

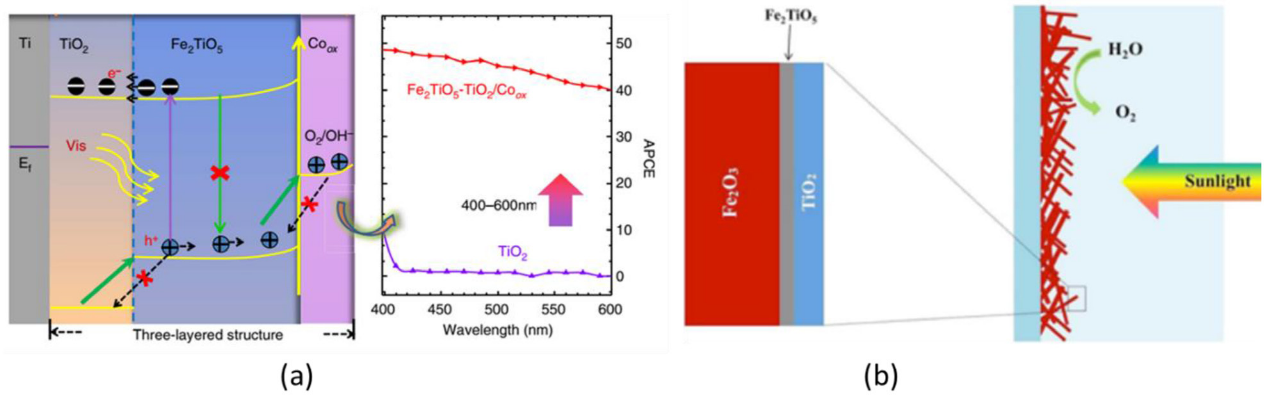

Figure 12. (a) Schematic representation of alignment between conduction band of TiO_2 and Fe_2TiO_5 along with APCE for the integrated system presented by Liu *et al*. [148] © 2014 Macmillan Publishers Limited. All rights reserved. With permission of Springer, (b) schematic diagram of Fe_2O_3 coupled with Fe_2TiO_5 presented by Deng *et al*; Reprinted with permission from [144]. Copyright (2015) American Chemical Society.

while the beneficial charge transport property of TiO_2 complemented the poor transport exhibited by Fe_2TiO_5. Such combination of TiO_2 and Fe_2TiO_5 has also been utilized as a photocatalyst for other water oxidation reactions [150, 151].

The band levels measured by UPS (figure 10(b)) shows that the good alignment of Fe_2O_3 and Fe_2TiO_5 bands could enhance electron/hole separation due to their favourable band level offset. Deng *et al* produced such a heterojunction structure by depositing a thin TiO_x layer on Fe_2O_3 photoanodes and post annealing it to convert the TiO_x layer into Fe_2TiO_5 (shown in figure 12(b)). The ultrathin Fe_2TiO_5 overlayer was fabricated by this solid-state reaction between Fe and Ti based oxides and hence limits the achievable thickness of Fe_2TiO_5. The Fe_2TiO_5 layer was amorphous as confirmed by Synchrotron-based soft x-ray absorption spectroscopy. This structure is a thin heterojunction between Fe_2O_3 and Fe_2TiO_5 which appears to have improved the charge separation.

Courtin *et al* demonstrated nano heterostructured photoanodes synthesized via a sol gel synthesis method based on Fe_x–TiO_2 with varied Fe content in TiO_2 [152]. They obtained the best photocurrent for films corresponding to $x = 0.2$, which contained Fe-doped anatase, pseudobrookite, and traces of hematite. Since the major phase in the product was pseudobrookite, it was proposed that it forms an intermediate conduction level between TiO_2 and Fe_2O_3 and electron transfer is facilitated from Fe_2TiO_5 to Fe_2O_3. Lately, doping of Ti in Fe_2O_3 has been tried by Lin *et al* where they demonstrated electrodeposition of Fe_2TiO_5 nanostructures [153]. When employed in water oxidation, this structure gave four fold enhanced the photocurrent density relative to pristine hematite. Such enhancement was attributed to local heterojunctions of Fe_2TiO_5 with Fe_2O_3 which probably decreased the hole accumulation.

Aforementioned heterojunctions either consisted of nanoscale junctions or comprised of ultrathin Fe_2TiO_5 overlayers produced by solid-state reaction. While the former possibility is lacking the necessary quantitative information of the phases for further investigations, the latter possibility implies a Fe_2TiO_5 layer whose thickness is limited by the diffusion of Fe and Ti and may result in irregular thickness or mixed phases of oxides. Our group reported an all-crystalline heterojunction of Fe_2TiO_5 with Fe_2O_3 by a hydrothermal route which facilitates a distinct and tunable electrical junction [154]. This was to facilitate efficient electron and hole transport to back contact and electrolyte respectively by forming a crystalline type II band alignment (as shown in figure 13(a)). FeOOH nanorods grown on FTO substrate by a hydrothermal route were used for sequential solvothermal synthesis of Fe_2TiO_5 nanoparticle based film on top of the nanorods followed by thermal treatment. An appreciable photocurrent density of 1.4 mA cm^{-2} was achieved through the heterojunction as opposed to low photocurrent density of 0.01 mA cm^{-2} demonstrated by the pristine Fe_2O_3 nanorods (figure 13(b)). Through Electrochemical Impedance Spectroscopy (EIS), values of charge transfer resistance through surface states and space charge capacitance were extracted. The coincidence of the peak of C_{ss} and the valley of $R_{ct,ss}$ with the jump in photocurrent density with increasing potential for optimized heterojunction (grey curve), as shown in figure 13(c), supports the viability of the model fitted for EIS. The model suggests that the photogenerated hole transfer into the electrolyte occurs through the surface states. The schematic representation of the 2 step hole transfer mechanism is shown in figure 13(d). Blue curve shows the first step of holes getting trapped at surface states and the red curve is the subsequent step of injection of trapped holes into the electrolyte. High surface charge separation efficiency of 85% indicated the role of Fe_2TiO_5 in enhancing hole injection into the electrolyte. The onset potential shifted by 30 mV to 0.9 V_{RHE} and a photocurrent of 1.6 mA cm^{-2} was attained through coupling with CoO_x cocatalyst.

Wang *et al* reported a 4 to 8 times increase in the water oxidation photocurrent for Fe_2O_3/Fe_2TiO_5 system with a significant cathodic shift of the onset potential of up to 0.53–0.62 V_{RHE} [155]. The performance of this heterostructure was further improved by decoration of the surface with a SnO_x layer owing to the synergistic effect of passivation of surface states by the latter. Li *et al* exhibited a 3D Fe_2O_3/Fe_2TiO_5 heterojunction photoanode synthesized by a hydrothermal technique [156]. The titanate layer was formed using ALD on the core FeOOH followed by high temperature annealing. After

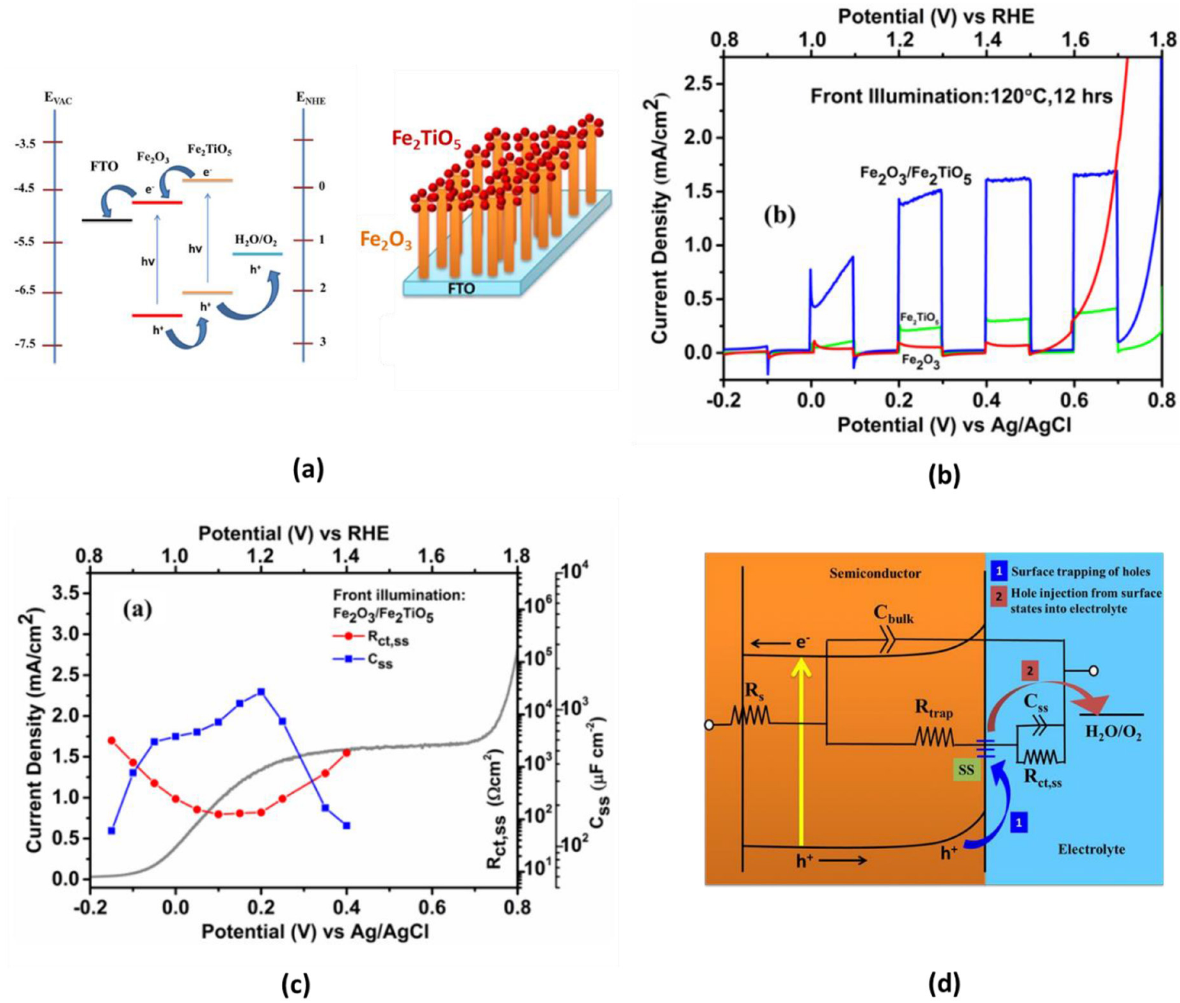

Figure 13. (a) Schematic representation of band offset and heterojunction nanorods of Fe_2O_3/Fe_2TiO_5 system; (b) chopped *J–V* curve, (c) linear sweep voltametry with surface state capacitance (C_{ss}) and resistance through surface states ($R_{ct,ss}$) and (d) proposed hole transport model for optimized heterojunction. Reprinted from [154], Copyright 2016, with permission from Elsevier.

coupling with $FeNiO_x$ cocatalyst, it yielded a photocurrent density of around 2.7 mA cm^{-2} at 1.23 V_{RHE} with an onset potential of 0.8 V_{RHE}. This is similar to our earlier work on ALD deposited TiO_x ultrathin overlayer on FeOOH nanorods [108]. As opposed to the high temperature of 750 °C used by Li *et al*, we kept our annealing temperature to 650 °C to avoid the degradation of FTO and to control Sn diffusion from FTO substrate to hematite. We established that the surface passivation by the TiO_x overlayer was responsible for the higher performance as compared to pristine Fe_2O_3 nanorods. Very recently, Wang *et al* demonstrated a PEC device with three components Fe_2TiO_5/Fe_2O_3/Pt heterostructure with enhanced light harvesting through Pt nanoparticles [157]. This also had a synergistic charge transfer between hematite film and Fe_2TiO_5 outer shell as well as with Pt underlayer. On the one hand, Fe_2TiO_5 shell improved the hole transfer to the surface; on the other, Pt nanoparticles worked as an electron transfer mediator and a light trapping element. They achieved a photocurrent of 1 mA cm^{-2} at 1.23 V versus RHE under AM 1.5G illumination.

Some other reports have used different modifications and treatments to improve the surface of Fe_2O_3/Fe_2TiO_5. Lv *et al* reported hydrothermal deposition of FeOOH on pre-treated FTO substrates, modified with titanium and phosphorous, which resulted in Ti and P modified hematite hollow nanostructures after annealing [158]. They demonstrated that P modified hematite with Fe_2TiO_5 incorporated yielded the highest photocurrent density of 2.37 mA cm^{-2} at 1.23 V_{RHE}. It was proposed that Fe_2TiO_5 improves charge separation with Fe_2O_3 while $FePO_4$ enhances the hole transfer on the surface. This was further improved by coupling it with Co–Pi cocatalyst to achieve 2.9 mA cm^{-2} at 1.23 V_{RHE}. Deng *et al* demonstrated F and Rh based treatments on Fe_2O_3/Fe_2TiO_5 system to lower the onset potential [159]. The photoanode system was fabricated by dip coating FeOOH nanorods in $TiCl_4$ solution. The treatment of fluorine and subsequent immersion in NaOH solution improved the semiconductor/electrolyte interface by forming a hydrogen bond network. The hole transfer was enhanced by partial reduction of surface Fe atoms. Coupling the system with Rh based cocatalyst resulted in a photocurrent density of 1.47 mA cm^{-2} at 1.0 versus RHE. More importantly, this yielded a final onset potential of 0.63 V versus RHE which is comparable to the lowest reported value for hematite. Such work has been reported by Tang

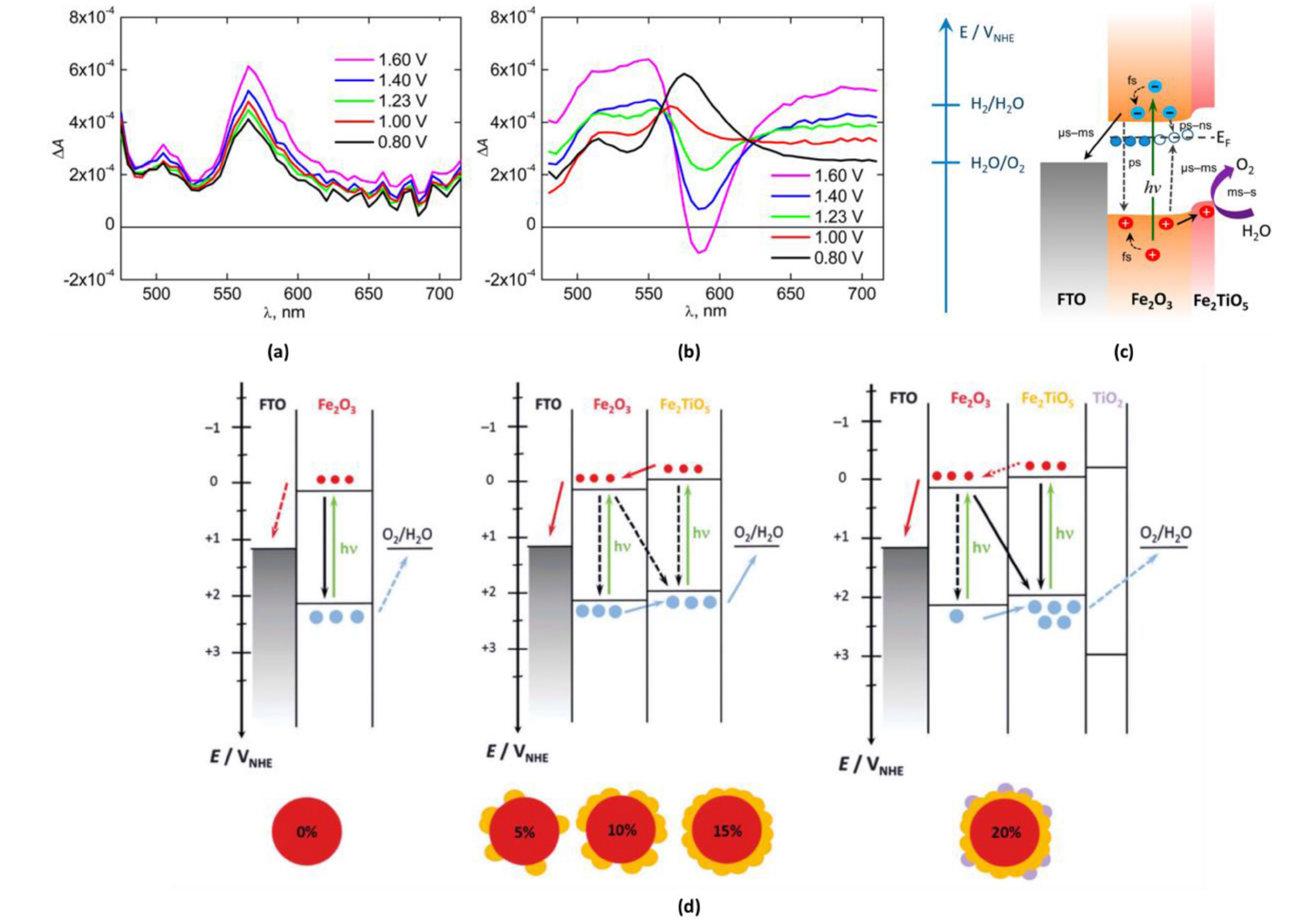

Figure 14. (a) Longest decay component spectra ($\tau > 5$ ns) from picoseconds to nanoseconds TAS for the (a) bare hematite and (b) hematite–titania (15% TiO_2) photoanodes at different bias voltages versus RHE; (c) Schematic representation of charge generation, recombination, and transfer in the nanocomposite photoelectrodes; Reprinted with permission from [163]. Copyright (2015) American Chemical Society, and (d) thermodynamic scheme of the charge generation, transfer and recombination processes at the biased (1.23 V_{RHE}) semiconductor electrolyte interface (SEI) under illumination and for different titania doping levels, including: no doping (0%, left), intermediate and optimum doping (5%–15%, center) and large doping (20%, right). Reproduced from [164] with permission of The Royal Society of Chemistry.

et al who discussed the interfacial coupling effect in quaternary hematite composite [160]. A photocurrent of 2.2 mA cm^{-2} was achieved for the integrated photoanode ITO/Fe_2O_3/Fe_2TiO_5/FeNiOOH multi-layer nanowires. It was designed with ITO underlayer to improve the electron conductivity to the back contact, Fe_2TiO_5 coating as energy level modulator and FeNiOOH nanodot catalyst to improve the interfacial hole transfer through regulating surface states energy level. The design presented by them appears to be complete in targeting different limitations of the device but further improvement by even more intense optimization is still needed.

Recently, Shuai *et al* demonstrated preparation of hematite and ultrathin iron titanate layer via an *in situ* reaction which yielded, the highest photocurrent density for Fe_2O_3/Fe_2TiO_5 heterojunction systems of around 3.05 mA cm^{-2} at 1.23 V versus RHE after employing a CoPi catalyst on top [161]. They presented a strategy to avoid going through the route of depositing FeOOH film by using an electro-reduction (ER) technique. This was done to prevent the undesirable microstructural defects created by the complexes and the bridging ligands formed by Fe^{+3} species in the solution during FeOOH growth. IMPS and Mott-Schottky results corroborate that the electron migration to the back contact was better for such systems than those prepared by FeOOH route. A stable performance was shown for 60 h in the integrated system where the photocurrent density remained at 98.9% of the initial value at the completion of test. A similar Fe_2O_3/Fe_2TiO_5 heterojunction, coupled further with TiO_2, was also used for the removal of some organic pollutants through photo fenton reaction (PFR) [162]. This triple heterojunction structure demonstrated much higher and stable PFR activity for the degradation of Methyl Orange than the catalysts of Fe_2O_3 and TiO_2/Fe_2O_3.

4.2. Understanding the charge dynamics of Fe_2O_3/Fe_2TiO_5 heterojunction

Since Fe_2O_3/ Fe_2TiO_5 heterojunction composite has proven to be a promising photoanode system with good performance and stability, it is necessary to understand its internal charge dynamics. The Fe_2O_3/Fe_2TiO_5 heterojunction has been

Table 4. List of hematite based heterostructures with iron based oxides as photoanodic system.

Base heterojunction	Preparation technique	Photocurrent density with electrolyte	Modified with underlayer/doping/overlayer/cocatalyst	Refs.
Fe_2O_3/Fe_2TiO_5	HF assisted Ti treatment of FeOOH followed by annealing	2.6 mA cm^{-2} at 1.23 V_{RHE}—1M NaOH	Coupled with CoPi cocatalyst	[144]
Fe_2O_3/Fe_2TiO_5	Hydrothermal grown FeOOH with solvothermal grown Fe–Ti–O layer followed by thermal treatment	1.6 mA cm^{-2} at 1.23 V_{RHE}—1M NaOH	CoO_x cocatalyst	[154]
Fe_2O_3/Fe_2TiO_5	Fe_2O_3 based nanoflakes achieved by thermal oxidation of Fe foils followed by solution chemistry	1.0 mA cm^{-2} at 1.23 V_{RHE}—1M KOH	Coated with SnO_x overlayer	[155]
Fe_2O_3/Fe_2TiO_5	Hydrothermal grown FeOOH and then ALD coating of TiO_x followed by thermal treatment	2.7 mA cm^{-2} at 1.23 V_{RHE}—1M KOH	Decorated with $FeNiO_x$ cocatalyt	[156]
Fe_2O_3/Fe_2TiO_5	Solution based Fe2O3 with dip coating of $TiCl_4$	1.0 mA cm^{-2} at 1.23 V_{RHE}—1M KOH	Pt nanopillars as underlayer	[157]
Fe_2O_3/Fe_2TiO_5	Hydrothermal technique with induction of Ti and P	2.90 mAcm^{-2} at 1.23 V_{RHE}—1M NaOH	Surface modification with phosphorous and Co–Pi catalyst	[158]
Fe_2O_3/Fe_2TiO_5	Hydrothermal grown Fe_2O_3 with dip coating of $TiCl_4$	2.12 mA cm^{-2} at 1.23 V_{RHE}—1M NaOH	F treated sample with Rh-based cocatalyst	[159]
Fe_2O_3/Fe_2TiO_5	Hydrothermal grown FeOOH nanowires treated with Atomic Layer Deposited Ti layer	2.2 mA cm^{-2} at 1.23 V_{RHE}—1M NaOH	DC sputtered ITO underlayer and FeNiOOH electrocatalyst	[160]
Fe_2O_3/Fe_2TiO_5	Fe_2O_3 deposited by electro reduction followed by Ti coating and thermal treatment	3.05 mA cm^{-2} at 1.23 V_{RHE}—1M NaOH	Integrated with CoPi cocatalyst	[161]
Mg doped Fe_2O_3/Doped Fe_2O_3	Atomic layer deposited	0.25 mA cm^{-2} at 1.0 V_{RHE}—1M KOH	Mg doped Fe_2O_3	[173]
$Fe_2O_3/Fe_xSn_{1-x}O_4$	Hydrothermal followed by drop casting of $SnCl_4$	2.25 mA cm^{-2} at 1.23 V_{RHE}—1M NaOH	SnO_x Overlayer converted to $Fe_xSn_{1-x}O_4$ through solid state diffusion	[64]
$CaFe_2O_4/Fe_2O_3$	Hydrothermal grown	0.53 mA cm^{-2} at 1.23 V_{RHE}—1M KOH	p-n heterojunction with Co–Pi catalyst	[168]
$Fe_2O_3/ZnFe_2O_4$	Spin coating	0.44 mA cm^{-2} at 0.2 $V_{Ag/AgCl}$—0.1M Glucose and 0.5 M NaOH (pH = 13.0)	Surface treatment with $ZnFe_2O_4$ precursor solution	[169]
$Fe_2O_3/ZnFe_2O_4$	Ultrasonic spray pyrolysis	2.19 mA cm^{-2} at 1.23 V_{RHE}—1M NaOH	Nanospikes based 3D textured substrate	[165]
Ti doped $Fe_2O_3/ZnFe_2O_4$	Hydrothermal grown Ti doped Fe_2O_3 with surface treated ZnO	0.3 mA cm^{-2} at 1.23 V_{RHE}—1M KOH	Ti doped Fe_2O_3	[166]
Co doped Fe_2O_3/Mg-Fe_2O_4	Hydrothermal and wet impregnation	3.34 mA cm^{-2} @ 1.40 V_{RHE}—0.01M Na_2SO_4	Co doped Fe_2O_3	[167]

Table 5. Hematite photoanode with various conducting scaffold for water oxidation.

Templates	Photocurrent density (mA cm^{-2})	Potential versus RHE	IPCE @ V versus RHE	Electrolyte	References
ITO inverse opal	1.60	1.53	18% @ 350 nm and 1.53 V	1M NaOH	[180]
AZO nanotubes	1.10	1.40	27% @ 400 nm	1M NaOH	[181]
rGO scaffold	1.06	1.23	Not Provided	1M NaOH	[182]
CNT	4.50	1.23	90	1M NaOH	[183]
Gr-CNT	0.32	1.23	7% @ 400 nm	1M NaOH	[175]
$TiSi_2$ nanonet	1.60	1.23	46% @ 400 nm	1M NaOH	[174]
N-doped graphene	1.06	1.23	130	1M NaOH	[184]
Gaphene/$BiV_{1-x}Mo_xO_4$	0.23	1.50	Not provided	0.01M Na_2SO_4	[185]
Inverse opal TiO_2	1.30	1.23	Not provided	1M NaOH	[186]

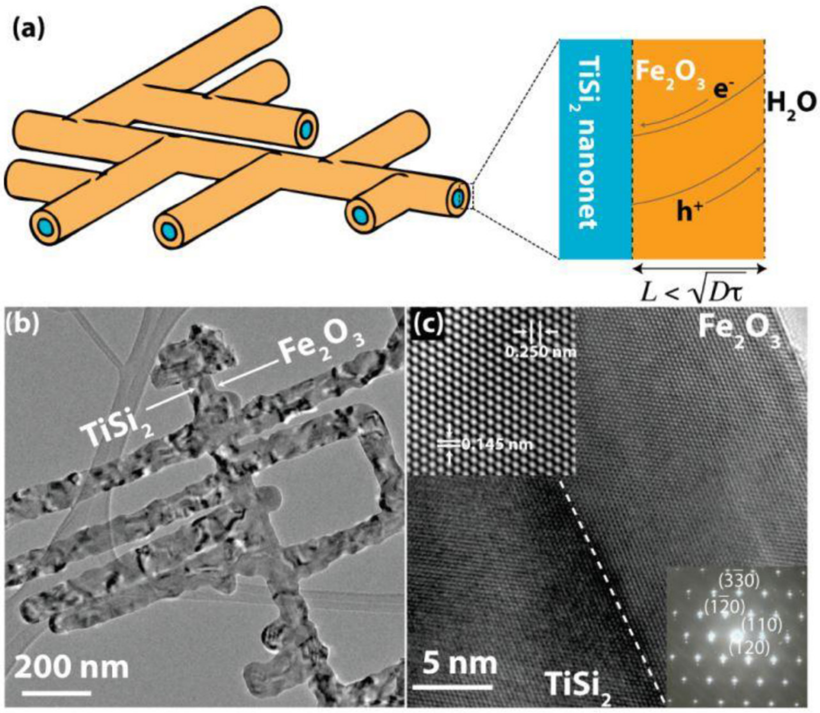

Figure 15. (a) Architecture of a conductive $TiSi_2$ nanonet in hematite for effective charge collection. The electronic band structure is shown in the enlarged cross-sectional view. (b) TEM image of $TiSi_2$-hematite core–shell. (c) HRTEM image of $TiSi_2$-hematite core–shell. The dashed line is the interface. Reprinted with permission from [174]. Copyright 2011 American Chemical Society.

investigated using a variety of spectroscopic techniques and it seems that this junction promotes the fast decay of accumulating holes leading to better charge carrier kinetics. A detailed exploration of the charge carrier kinetics in such systems was carried out by Ruoko *et al* through transient absorption spectroscopy (TAS) on hematite–titania nanocomposite photoanodes, from sub-picosecond to second time-scale [163]. It was suggested that hole transport efficiency can be evaluated by observing fast electron trapping to localized oxidized states near the conduction band edge of hematite which competes with electron hole pair recombination. Hence, longest time scale (>5 ns) resolved TAS was obtained under different bias through picoseconds–nanoseconds TAS for hematite–titania photoanodes and bare hematite for comparison. As shown in figure 14(a), absorption feature at 580 nm remains unchanged with changing bias voltages for bare hematite and hence no electron trapping was observed. On the other hand, for the hematite–titania photoanode (shown in figure 14(b)), electron trapping to oxidized electron states is prominent at 580 nm with biases higher than onset voltage. This is attributed to increased charge separation due to the formation of the pseudobrookite–hematite heterojunction. The presence of titania affected the charge separation positively by increasing the number of long lived holes with an average accumulation lifetime of 0.4 ± 0.1 s. In comparison, long-lived holes in bare hematite photoanode were much less adversely affecting the performance. The decay of the long-lived holes is one order of magnitude faster in the composite photoanodes than previously published for doped hematite, indicative of higher catalytic efficiency. This study on different lifetime scales for recombination, electron trapping and hole transport mechanisms in hematite–titania photoanodes (shown in figure 14(c)) reaffirmed the importance of titania junction in improving the hole transport and corroborated that bare

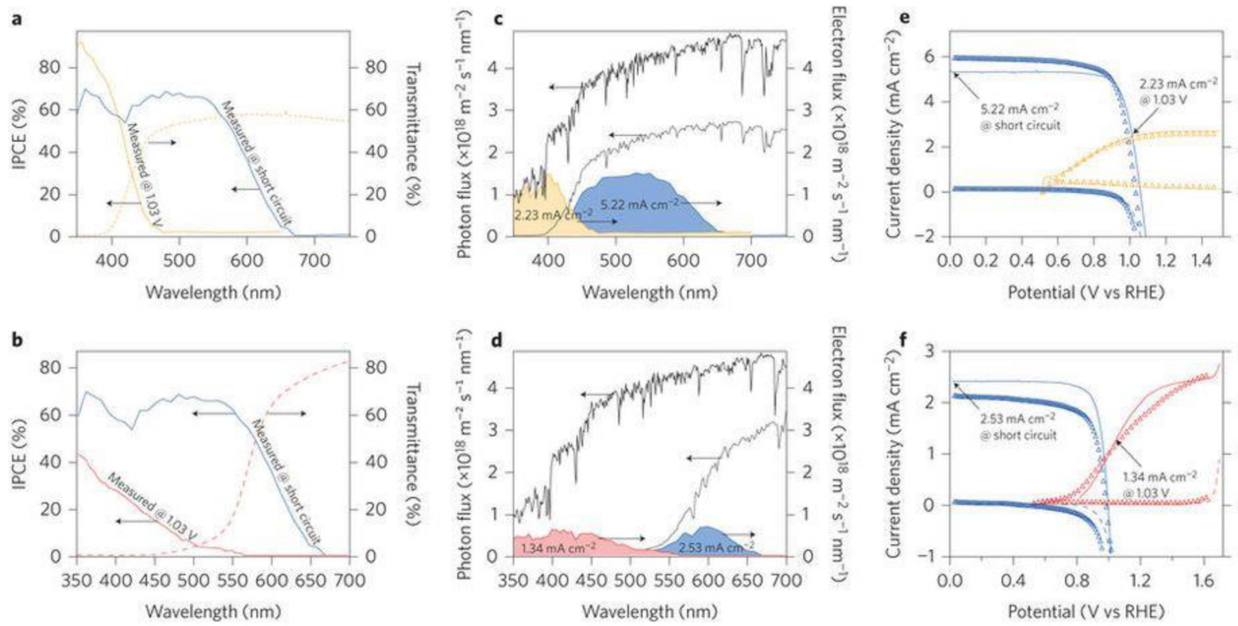

Figure 16. (a)–(f) Spectral response and *J–V* characteristics of the WO_3 (yellow)/DSC (blue) ((a), (c) and (e)) and Fe_2O_3 (red)/DSSC (blue) (b,d,f) tandem cells. The transmittance of the photoanode ((a) and (b) dashed lines) convoluted to the AM 1.5G photon flux on the photoanode ((c) and (d) black lines) allows the photon flux incident at the DSC to be calculated ((c) and (d), grey lines). IPCE data (a,b, solid lines) and the photon flux incident at each element are used to estimate the photocurrent density (shaded areas under the curves in (c) and (d)). *J–V* curves ((e) and (f)) of the cells are shown under AM 1.5G irradiation. Solid lines represent the *J–V* curves predicted from calculation. [192] © 2012 Macmillan Publishers Limited. All rights reserved. With permission of Springer.

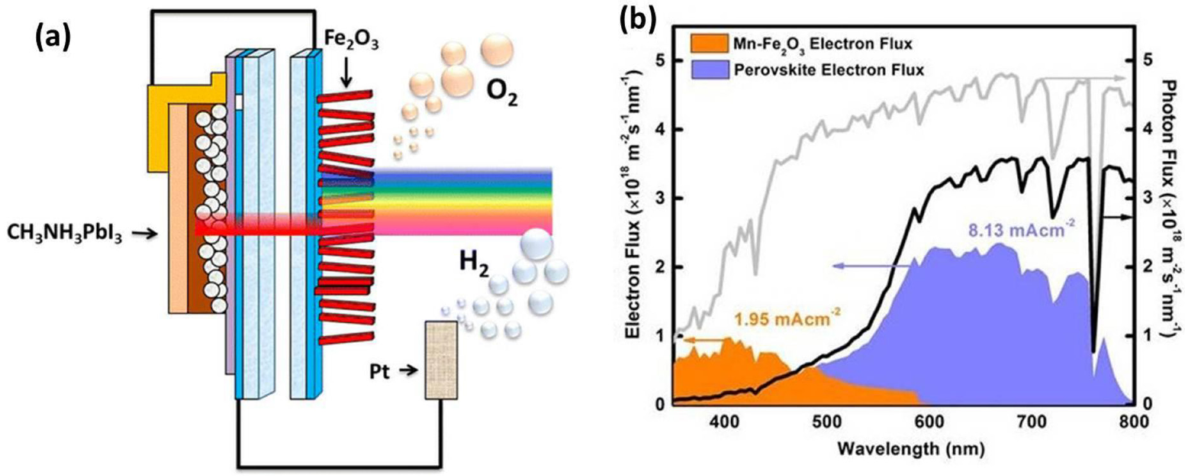

Figure 17. Hybrid photovoltaic and PEC tandem approach of Gurudayal *et al* for overall water splitting at an efficiency of 2.4%. A $CH_3NH_3PbI_2$ solar cell was used to bias an oxygen evolving Fe_2O_3 photoanode. Reprinted with permission from [35]. Copyright 2015 American Chemical Society.

hematite possesses poor charge dynamics that limits its performance as a photoanode.

Damián *et al* studied the interfacial charge transfer in hematite–titania system with titania concentrations ranging from 0% to 20% (as shown in figure 14(b)) [164]. Solid state diffusion and interface reactions lead to an Fe_2TiO_5 shell with core as Fe_2O_3. They observed that an optimum condition was obtained for 10% titania concentration due to an efficient transfer of holes from hematite to pseudobrookite and electrons from pseudobrookite to hematite. At higher concentration of TiO_2, an unreacted TiO_2 layer exists which prevents efficient hole transfer by increasing recombination in the Fe_2TiO_5 layer, and hence inhibits water photooxidation. This is referred to as a 'hole mirror' mechanism. The charge transfer mechanism revealed by EIS shows hole trapping at the surface states before transferring into water as discussed in our earlier report [154].

4.3. Hematite based heterostructures with other metal oxides

Hematite based heterojunctions have been reported with other iron based metal oxides like spinel ferrites as well [165–169]. A comprehensive list of hematite based heterostructures is given in table 4 which includes those already discussed in

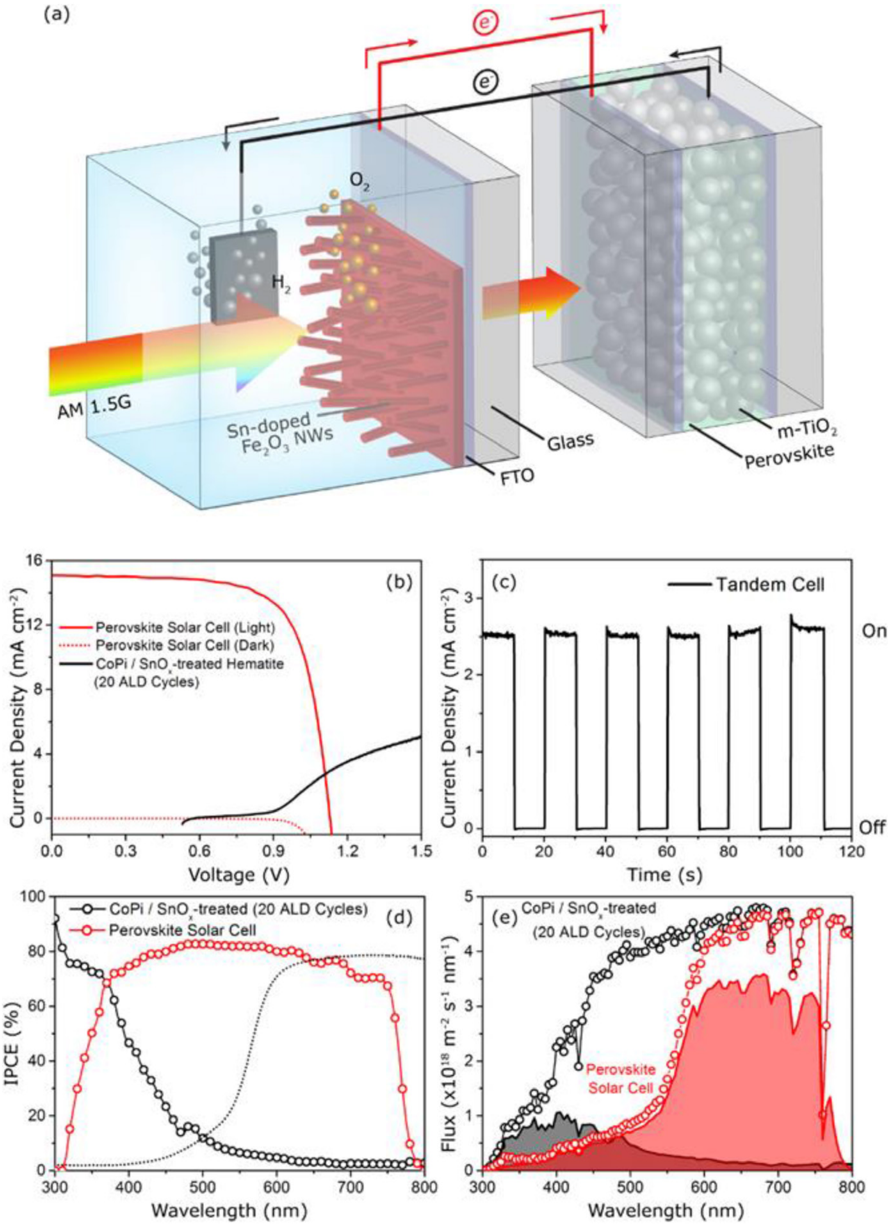

Figure 18. (a) Schematic of tandem cell featuring a perovskite solar cell and CoPi/20C hematite photoanode, (b) Current–voltage curve of a perovskite solar cell—CoPi/SnO_x treated (20 ALD cycles) hematite photoanode tandem devices together under standard AM 1.5G irradiation, (c) I–t curve of tandem cell (TS) in 1M NaOH electrolyte under 1 Sun AM1.5G (100 mW cm^{-2}) up to 120 s, (d) IPCE spectra of CoPi/SnO_x treated (20 ALD cycles) hematite photoanodes and perovskite solar cell at 1.15 V versus RHE and at short circuit condition respectively and (e) standard solar AM 1.5G photon flux and incident photon flux for solar cell calculated by multiplying the standard photon flux by the transmittance of the CoPi/SnO_x treated (20 ALD cycles) hematite. The shaded areas are electron flux from CoPi/SnO_x treated (20 ALD cycles) hematite and perovskite solar cell used to calculate the integrated photocurrent density. [24] John Wiley & Sons. © 2017 Wiley-VCH Verlag GmbH & Co. KGaA, Weinheim.

sections 4.1 and 4.2 on Fe_2O_3/Fe_2TiO_5 heterostructure. An interesting heterostructure was reported by Hussain *et al* in $ZnFe_2O_4$/Fe_2O_3 composite deposited on a 3D nanospikes substrate by spray pyrolysis [165]. This film exhibited a photocurrent density of 2.9 mA cm^{-2} at 1.23 V_{RHE} and is attributed to better charge conductivity as evidenced by EIS. Hou *et al* reported a photocurrent density of 3.34 mA cm^{-2} at 1.40 V_{RHE} for a tree like branched structure which comprised of heterojunctions between a Co-doped Fe_2O_3 nanorod array as core and $MgFe_2O_4$ spinel as shell [167]. The nanorods array was deposited by a hydrothermal route on Ti mesh and was followed by coating $MgFe_2O_4$ through wet impregnation. $FeVO_4$ has also been coupled with Fe_2O_3 as a direct z-scheme structure for photoelectrochemistry [170]. Zhang *et al* recently investigated $FeVO_4$ based photoanodes and discussed their intrinsic optoelectronic properties [171]. In addition, Li *et al* used $FeVO_4$/Fe_2TiO_5 composites for the photocatalytic removal of norfloxacin [172]. Another strategy to form a heterojunction is by doping hematite to alter its properties. Lin *et al* doped hematite with Mg to invert its naturally n-type nature to p-type and reported a p-n homojunction fabricated by ALD [173]. Importance of Sn^{+4} infusion was reported by our group where photocurrent density of 2.25 mA cm^{-2} at 1.23 V_{RHE} was achieved in SnO_x coated Fe_2O_3 nanorods [64]. The formation of complex $Fe_xSn_{1-x}O_4$ phase after the thermal treatment was thought to improve the charge separation in this photoanode device.

5. Hematite integrated with conducting scaffolds

Another efficient approach to enhance the charge separation efficiency of hematite is to incorporate electron conducting scaffolds into the hematite nanostructure (table 5). During illumination, electrons from the photo generated charge carriers can be collected by the conductive scaffolds and readily transported away to the current collector while holes are transferred to the semiconductor–liquid junction to oxidize water.

A good example of a hematite anode with an embedded conducting scaffold was demonstrated by Lin *et al* (figure 15) [174] which used high surface area $TiSi_2$ nanonet as the conducting scaffold for efficient charge collection which also played the additional role of being a structural support to hematite. In such a composite nano structure architecture the distance from any point in the hematite to the electrode/electrolyte interface can be made shorter than the charge-diffusionlength, allowing efficient charge collection. They reported an external quantum efficiency of 46% at 400 nm wavelength without any intentional doping of hematite in a water-splitting environment.

Graphene is another material recognized as a good electron collector and transporter. Use of graphene as a charge collecting scaffold could effectively prevent recombination of photogenerated electron–hole pairs resulting in improved photocatalytic conversion efficiency [175, 176]. Yoon *et al* demonstrated this charge collection enhancement experimentally in a graphene coupled hematite system [177]. Meng *et al* also demonstrated the benefit of graphene as a charge collector in an anode where hematite nanoparticles were added onto reduced graphene oxide (rGO) nanosheets [178]. Similarly, carbon nanotubes (CNTs) have also been used as charge separation scaffolds when combined with the hematite photoanode [175]. Kim and coworkers reported hematite photoanode coupled with multi-walled CNTs which exhibited 66% boost in photocurrent relative to plain hematite photoanode [175]. Multi-walled CNT also served as a structural support to hematite nanoparticles.

Finally, more efforts in using a conducting scaffold or heterostructure with hematite coating layer could be pursued to efficiently extract the photogenerated carriers from hematite. An example of successful demonstration by this approach is the $WO_3/BiVO_4$ core shell structure which gave a photocurrent density of 6.8 mA cm^{-2} which is 90% of the theoretical limit of photocurrent of $BiVO_4$ [179].

6. PEC-PV tandem approach with hematite based photoanode.

Single material photoanodes cannot generate the required photovoltage (1.6–1.8 V) to split water even if all the above-mentioned modifications are successfully incorporated. Therefore, a bias voltage is always required. Here, we will discuss a different approach of tandem cell design that could generate enough photo voltage to drive water-splitting reaction without an external bias.

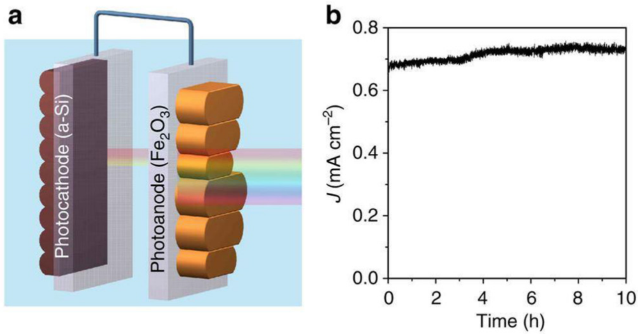

Figure 19. (a) Schematics of hematite photoanode and amorphous Si photocathode in a tandem configuration of overall unassisted water splitting. (b) Total photocurrent during the first 10 h of operation using $NiFeO_x$-modified rgH II with TiO_2/Pt-loaded amorphous silicon photocathode in 0.5M phosphate solution (pH 11.8) in a two-electrode, tandem configuration (no external bias). Reproduced from [93].

Soon after the discovery of tandem photovoltaic cells by Fujishima and Honda, it was realized that this approach of additive voltages could be exploited for efficient solar water splitting too [8]. The theoretically calculated efficiencies for these types of tandem approaches can be >25% depending on the illumination conditions (i.e solar concentration) and catalyst overpotentials used in the simulations [187, 188]. General reviews of tandem approaches for solar to hydrogen conversion have been published recently [20, 188–190]. Hence, we will focus specifically on hematite based tandem devices for solar water splitting

A tandem cell configuration (PEC-PV) is where the total photovoltage required to split water is generated by optical absorption in two or more series connected photoabsorbers [24, 35, 191]. Some of the absorbers could be photo active electrodes while a series connected solar cell could also be one. Sivula *et al* reported Fe_2O_3/2-series connected DSSC solar cells and WO_3/2-series connected DSSC solar cells in tandem configuration for solar assisted overall water splitting (figure 16) [192]. The WO_3/DSSC tandem device achieved a STH conversion efficiency η_{STH} of up to 3.10% (this is ~50% of the maximum efficiency obtainable with this material: $\eta_{STH,max} = 6.24\%$, assuming Eg = 2.6 eV), whereas the Fe_2O_3/DSSC tandem device gave only $\eta_{STH} = 1.17\%$ (less than 8% of its maximum: $\eta_{STH,max} = 16\%$ with Eg = 2.1 eV) needing significant improvement [192].

The photovoltage outputs (V_{OC}) of the solar cells are crucial in these tandem devices. The photovoltage generated by traditional solar cells i.e. silicon, CIGS and DSSC is not enough to drive water splitting reaction solely [93, 193–196]. The relatively large open circuit voltages generated by halide perovskites could make them attractive candidates as the photovoltaic components of solar fuel devices [197–199]. Our group fabricated a hematite–perovskite tandem cell which gave STH conversion efficiency of 2.4% (figure 17) [35].

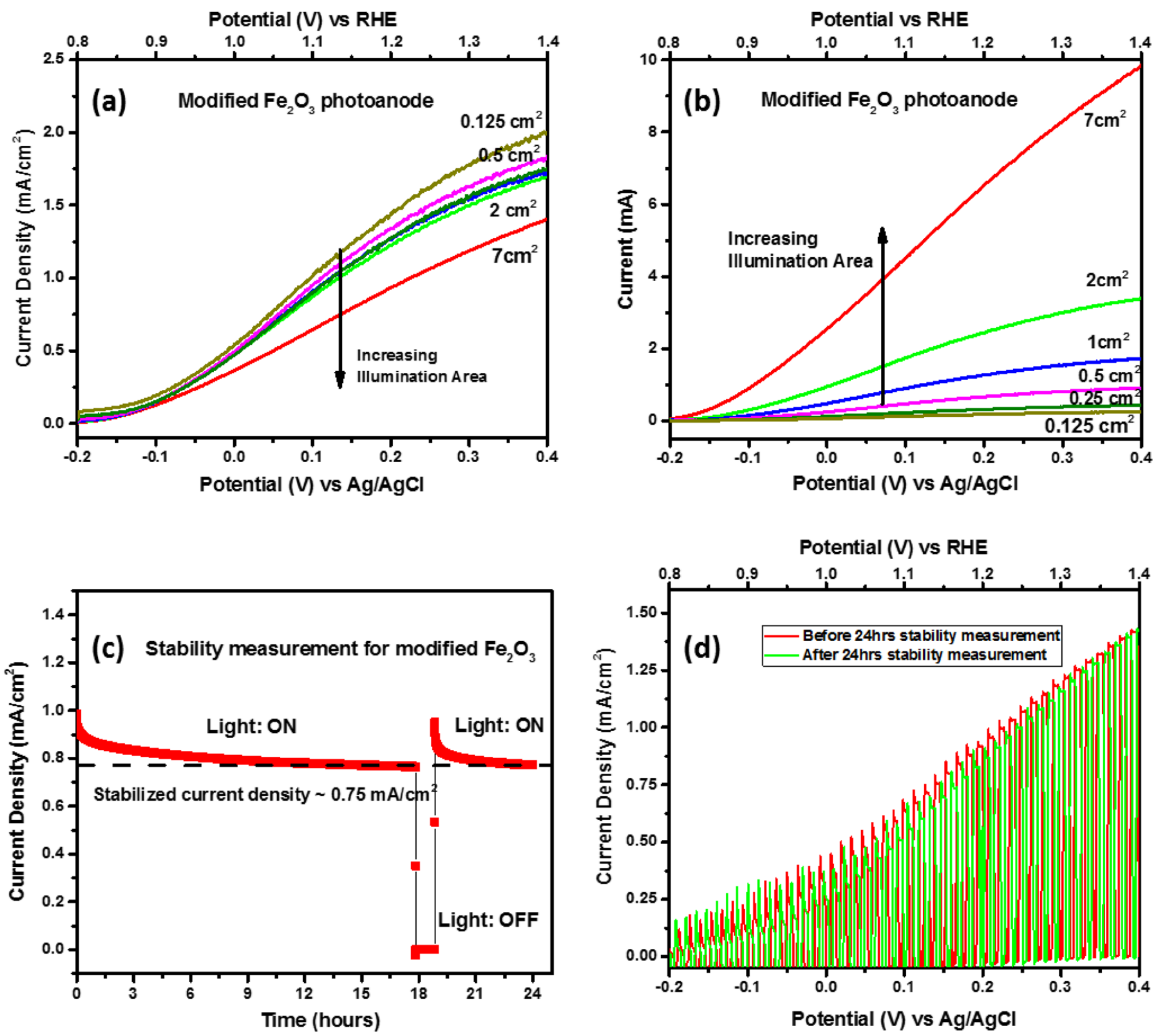

Figure 20. (a) Current density (J), and (b) current, versus potential (V) curve for large area modified hematite devices under different illumination areas, (c) stability test and (d) J–V plots before and after the measurement of modified large area hematite based devices with 7 cm^2 illumination. All measurements done under standard AM 1.5G irradiation in 1M NaOH (pH = 13.6).

The main limitation in this tandem cell was found to be the high onset potential of the hematite photoanode. However, the total photopotential generated by our tandem system was 1.87 V which exceeded both the thermodynamic and kinetic requirements for water splitting (1.6 V), resulting in successful splitting without the assistance of any electrical bias [35]. Gratzel *et al* also demonstrated an optically transparent $FeNiO_x$ cocatalyst coated hematite and perovskite tandem cell for solar assisted over all water splitting with a STH conversion efficiency of 2% [80]. Recently, we have produced a more efficient SnO_x treated hematite–perovskite tandem cell whose STH conversion efficiency reached 3.4% (figure 18) [24]. The ALD coating of SnO_x to hematite shows a dramatic enhancement in the performance of hematite. Sn acts both, as a dopant, as well as a surface passivation layer in hematite giving 3.12 mA cm^{-2} photocurrent density at 1.23 V versus RHE. A photoanode–photocathode tandem configuration by utilizing a hematite photoanode and a-Si photocathode was demonstrated by Dunwei Wang's group with a STH conversion efficiency of 0.91% (figure 19) [93]. This device was stable for 10 h although its performance was limited by the low photocurrent and high onset potential. The overall performance of this configuration was very low in comparison to other PV-PEC tandem configurations.

7. Initiative towards large area hematite based photoelectrochemical cell devices

To demonstrate the commercial viability of hematite based PEC devices, it is imperative to translate the developments to large area devices. Scaling up the size of the electrodes and PEC cell leads to a different set of limitations and challenges. It is evident that with increasing illumination area, the factors like higher resistance in the back contact FTO, limitations in mass transport of ions in the electrolyte and non-uniformity of films, come into play. For small area, hematite nanostructures have reached high performance with photocurrent density as high as 6 mA cm^{-2} at 1.23 V versus RHE [30]. However, not many have explored the large area devices with bigger illumination area. Grätzel *et al* demonstrated a large area device (10 cm × 10 cm) with an illumination area of 80 cm [2] which yielded a total photocurrent of 35 mA which translates to a current density of 0.43 mA cm^{-2} [69]. Cao *et al* reported large area preparation of porous Ag_3PO_4 photoanodes with a photocurrent density of around 4.32 mA cm^{-2} at 1 V versus Ag/AgCl (equivalent to 1.86 V versus RHE for pH 11.3 Na_3PO_4 electrolyte) with a 5 h successive PEC water splitting experiment [200]. We have been developing large area hematite photoanodes on FTO substrate consisting an illumination area of up to 7 cm [2]. To observe the effect of illumination area on the performance of PEC devices, we varied the illumination area as 0.125 cm^2, 0.25 cm^2, 0.5 cm^2, 1 cm^2, 2 cm^2 and 7 cm^2.

As can be observed in figure 20(a), the modified hematite nanorods yielded a photocurrent density of around 1 mA cm^{-2} at 1.23 V versus RHE and a total current of 7 mA for an illumination area of 7 cm^2 (figure 20(b)). The smaller areas yielded higher photocurrent densities reaching as high as 1.5 mA cm^{-2} for an illumination area of 0.125 cm^2. The photocurrent stability was assessed in the large area illumination (7 cm^2) as shown in figure 20(c). It is clear that a large drop, of the order of 10% to 0.9 mA cm^{-2}, is evident in the photocurrent within a few seconds from the start and the photocurrent density eventually tails off at about 0.78 mA cm^{-2} in 18 h. With an intermediary light on/off after 18 h, it was observed that the current followed a slightly sharper drop as compared to the start of the measurement. It is quite possible that this transient drop is due to a build-up of evolved O_2 and H_2 gases at the electrodes. A change in the performance of the photoanode was also eventually noted in subsequent PEC measurements (figure 20(d)). A slight drop in the onset behavior at early potential range of Fe_2O_3 nanorods anode is evident although, it remained intact at 1.23 V versus RHE. These interesting observations are the preliminary indications of remaining challenges in the realization of large area, hematite based photoanodes in PEC water splitting. There are several issues with large area photoanodes those limit the performance of hematite such as; (1) ohmic losses due to poor conductivity, (2) high temperature annealing requirement, (3) non-uniform nanostructures in large area photoanodes, (4) mass transport limitation. These issues have to be addressed to improve the performance of hematite photoanode and maintain the stability at large area. Resistance losses in large area hematite can be addressed by connecting small hematite panels in series and parallel. Mass transport can be addressed by mechanically rotating the electrolyte or having a flow cell.

8. Summary and outlook

Recent developments in Fe_2O_3 (hematite) based photoanodes for solar assisted water splitting in PEC devices are reviewed here. With a theoretical solar to hydrogen efficiency of ~15%, good stability in aqueous electrolyte environment and abundance, hematite has a good potential as the main material for photoanodes in solar water splitting. Its performance, however, is limited by poor charge transport properties and sluggish hole transport across the interface to electrolyte.

To compensate for the deficiencies of hematite and to further improve it, various combinations of many different approaches have been investigated by researchers over more than 10 years. These are summarized below.

(a) Nanostructuring to compensate for the poor minority carrier diffusion length which is a morphological manipulation to facilitate efficient hole diffusion to space charge region.
(b) Doping hematite with a suitable multi-valent element to increase its inherent bulk conductivity. Tetravalent elements such as Sn and Si seem to be the most effective in improving the bulk properties and are widely used by researchers. Other elements such as Ti, Ge and Ru and some divalent elements have also been examined.
(c) Integration with a transparent and efficient OER cocatalyst which is applied on the surface of hematite to improve the hole injection ability across the hematite-electrolyte interface. The cocatalysts IrO_x, CoPi and $NiFeO_x$ are effective in this respect.
(d) Use of a surface passivation layer to reduce charge recombination at the surface. TiO_2 has been found to be very effective in reducing surface charge recombination and hence has been a popular choice for a passivation layer. However, some reports indicate that TiO_2 deposited on the surface of hematite reacts to form Fe_2TiO_5 which is the true surface passivating material.
(e) Use of an electron conducting nanonet embedded in the hematite to efficiently collect electrons and transport them to the back conductor thereby reducing the chances of recombination. $TiSi_2$, graphene and CNTs have shown to be effective as the conducting nanonets giving beneficial effects on the anode performance.
(f) Fabricating heterostructure with hematite and another material which has appropriate conduction and valance band offsets with respect to water redox levels and the band edges of hematite. Compounds such as TiO_2, Fe_2TiO_5, $FeVO_4$, and spinels such as $ZnFe_2O_4$ have been combined with hematite and have been shown to improve the photocurrent density. This strategy has not been adopted widely by many workers possibly because of the difficulty in synthesizing such nanocomposite materials, but this could become a very effective technique.

The exact roles of the cocatalyst and surface passivation layers in improving the anode performance is not clear yet. For example, CoPi has been reported to improve catalytic activity by many groups, but some claim that it provides surface passivation also. The inconsistency among the reports regarding the operating mechanisms could be due to different deposition techniques employed by the researchers, which lead to different intrinsic properties of the hematite and/or the CoPi layer.

The pseudobrookite phase of Fe_2TiO_5 is another candidate material with similar electronic properties to hematite but with better surface transport characteristics so that holes could be extracted more efficiently. It could be a potential alternative to hematite. The basic electrical and optical properties of Fe_2TiO_5 are not well known to systematically design a photoanode based on this material. Heterojunctions of Fe_2O_3–Fe_2TiO_5 and nanostructures of Fe_2O_3 core with Fe_2TiO_5 shell have shown very encouraging preliminary results as photoanodes. Efforts in nanostructuring, doping, and using Fe_2TiO_5 as the shell for another semiconductor, or as a conducting scaffold, might be worth exploring in future.

The significant research efforts in the hematite based photoanode developments, which shone light on the benefits of modifications such as nanostructuring + doping + surface passivation + co-catalyst has increased the photocurrent densities to ~6 mA cm^{-2}, which is ~50% of its theoretical limit. Given the recent success in WO_3–$BiVO_4$ core–shell heterostructured photoanodes which gave about 90% of theoretical photocurrent density, we remain optimistic that with the right combination of strategies, hematite photoanodes will also be able to realize its theoretical photocurrent density in future.

Finally, the laboratory understandings and experiences must be translated into pilot scale PEC devices to demonstrate the commercial viability of the technology. Hematite photoanodes of active areas about 7 cm^2 have been fabricated and tested which show that the photocurrent density appears to decrease with increasing illumination area. The reasons for this must be understood and the phenomenon must be circumvented for successful commercial deployment of this technology.

Acknowledgment

The authors acknowledge the funding support from the CREATE Programme under the Campus for Research Excellence and Technological Enterprise (CREATE), which is supported by the National Research Foundation, Prime Minister's Office, Singapore; the Singapore-German Mobility 2014 and the Ministry of Education (MOE) Tier 2 Project (MOE2016-T2-1-030).

ORCID iDs

Gurudayal https://orcid.org/0000-0002-9245-2199
Lydia Helena Wong https://orcid.org/0000-0001-9059-1745

References

[1] IEA 2015 *I. E. A. Key World Energy Statics* (www.iea.org/publications/freepublications/publication/KeyWorld2017.pdf)
[2] BP 2016 Outlook to 2035. BP (www.bp.com/content/dam/bp/en/corporate/pdf/energy-economics/energy-outlook/bp-energy-outlook-2016-focus-on-north-america.pdf)
[3] Tachibana Y, Vayssieres L and Durrant J R 2012 Artificial photosynthesis for solar water-splitting *Nat. Photon.* **6** 511–8
[4] Barber J 2009 Photosynthetic energy conversion: natural and artificial *Chem. Soc. Rev.* **38** 185–96
[5] Pinaud B A *et al* 2013 Technical and economic feasibility of centralized facilities for solar hydrogen production via photocatalysis and photoelectrochemistry *Energy Environ. Sci.* **6** 1983–2002
[6] Lin Y, Yuan G, Liu R, Zhou S, Sheehan S W and Wang D 2011 Semiconductor nanostructure-based photoelectrochemical water splitting: a brief review *Chem. Phys. Lett.* **507** 209–15
[7] Grätzel M 2001 Photoelectrochemical cells *Nature* **414** 338–44
[8] Fujishima A and Honda K 1972 Electrochemical photolysis of water at a semiconductor electrode *Nature* **238** 37–8
[9] Murth A S N and Reddy K S 1984 Photoelectrochemical behaviour of undoped ferric oxide (α-Fe_2O_3) electrodes prepared by spray pyrolysis *Mater. Res. Bull.* **19** 241–6
[10] Feng X, Chen Y, Qin Z, Wang M and Guo L 2016 Facile fabrication of sandwich structured WO_3 nanoplate arrays for efficient photoelectrochemical water splitting *ACS Appl. Mater. Interfaces* **8** 18089–96
[11] Kim T W and Choi K-S 2014 Nanoporous $BiVO_4$ photoanodes with dual-layer oxygen evolution catalysts for solar water splitting *Science* **343** 990–4
[12] Yu Y, Zhang Z, Yin X, Kvit A, Liao Q, Kang Z, Yan X, Zhang Y and Wang X 2017 Enhanced photoelectrochemical efficiency and stability using a conformal TiO_2 film on a black silicon photoanode *Nat. Energy* **2** 17045
[13] Hu S, Shaner M R, Beardslee J A, Lichterman M, Brunschwig B S and Lewis N S 2014 Amorphous TiO_2 coatings stabilize Si, GaAs, and GaP photoanodes for efficient water oxidation *Science* **344** 1005–9
[14] Ruth M and Joseck F 2011 *Hydrogen Threshold Cost Calculation* (www.hydrogen.energy.gov/pdfs/11007_h2_threshold_costs.pdf)
[15] Miller E, Ainscough C and Talapatra A 2014 *Hydrogen Production Status 2006–2013* (www.hydrogen.energy.gov/pdfs/14005_hydrogen_production_status_2006-2013.pdf)
[16] Keable J and Holcroft B 2012 Economic and business perspectives *Photoelectrochemical Hydrogen Production* ed R van de Krol and M Grätzel (Berlin: Springer) pp 277–92
[17] Murphy A B, Barnes P R F, Randeniya L K, Plumb I C, Grey I E, Horne M D and Glasscock J A 2006 Efficiency of solar water splitting using semiconductor electrodes *Int. J. Hydrog. Energy* **31** 1999–2017
[18] Ohashi K, McCann J and Bockris J O M 1977 Stable photoelectrochemical cells for the splitting of water *Nature* **266** 610
[19] Shaner M R, McDowell M T, Pien A, Atwater H A and Lewis N S 2016 Si/TiO_2 tandem-junction microwire arrays for unassisted solar-driven water splitting *J. Electrochem. Soc.* **163** H261–4
[20] Prévot M S and Sivula K 2013 Photoelectrochemical tandem cells for solar water splitting *J. Phys. Chem.* C **117** 17879–93
[21] Qiu Y *et al* 2016 Efficient solar-driven water splitting by nanocone $BiVO_4$-perovskite tandem cells *Sci. Adv.* **2** e1501764
[22] Walter M G, Warren E L, McKone J R, Boettcher S W, Mi Q, Santori E A and Lewis N S 2010 Solar water splitting cells *Chem. Rev.* **110** 6446–73
[23] Gaillard N, Chang Y, Kaneshiro J, Deangelis A and Miller E L 2010 Status of research on tungsten oxide-based photoelectrochemical devices at the University of Hawai'i *Proc. SPIE 7770 Solar Hydrog. Nanotechnol.* **7770** 77700V
[24] Gurudayal *et al* 2017 Atomically altered hematite for highly efficient perovskite tandem water-splitting devices *ChemSusChem* **10** 2449–56
[25] Bassi P S, Chiam S Y, Dayal G, Barber J and Wong L H 2014 Hydrothermal grown nanoporous iron based titanate, Fe_2TiO_5 for light driven water splitting *ACS Appl. Mater. Interfaces* **6** 22490–5

[26] Kavan L and Grätzel M 1995 Highly efficient semiconducting TiO_2 photoelectrodes prepared by aerosol pyrolysis *Electrochim. Acta* **40** 643–52
[27] Kim J H, Jo Y, Kim J H, Jang J W, Kang H J, Lee Y H, Kim D S, Jun Y and Lee J S 2015 Wireless solar water splitting device with robust cobalt-catalyzed, dual-doped $BiVO_4$ photoanode and perovskite solar cell in tandem: a dual absorber artificial leaf *ACS Nano* **9** 11820–9
[28] Higashi M, Domen K and Abe R 2012 Highly stable water splitting on oxynitride TaON photoanode system under visible light irradiation *J. Am. Chem. Soc.* **134** 6968–71
[29] Zhong M *et al* 2017 Highly active GaN-stabilized Ta_3N_5 thin-film photoanode for solar water oxidation *Angew. Chem., Int. Ed. Engl.* **56** 4739–43
[30] Jeon T H, Moon G-H, Park H and Choi W 2017 Ultra-efficient and durable photoelectrochemical water oxidation using elaborately designed hematite nanorod arrays *Nano Energy* **39** 211–8
[31] Cornell R M and Schwertmann U 2004 Introduction to the iron oxides *The Iron Oxides* (New York: Wiley) pp 1–7
[32] Cornell R M and Schwertmann U 2004 Soils *The Iron Oxides* (New York: Wiley) pp 433–74
[33] Sivula K, Le Formal F and Grätzel M 2011 Solar water splitting: progress using hematite (α-Fe_2O_3) photoelectrodes *ChemSusChem* **4** 432–49
[34] Bassi P S, Dayal G, Wong L H and Barber J 2014 Iron based photoanodes for solar fuel production *Phys. Chem. Chem. Phys.* **16** 11834–42
[35] Dayal G, Sabba D, Kumar M H, Wong L H, Barber J, Grätzel M and Mathews N 2015 Perovskite–hematite tandem cells for efficient overall solar driven water splitting *Nano Lett.* **15** 3833–9
[36] Guo X, Wang L and Tan Y 2015 Hematite nanorods Co-doped with Ru cations with different valence states as high performance photoanodes for water splitting *Nano Energy* **16** 320–8
[37] Kim J Y, Magesh G, Youn D H, Jang J-W, Kubota J, Domen K and Lee J S 2013 Single-crystalline, wormlike hematite photoanodes for efficient solar water splitting *Sci. Rep.* **3** 2681
[38] Peerakiatkhajohn P, Yun J-H, Chen H, Lyu M, Butburee T and Wang L 2016 Stable hematite nanosheet photoanodes for enhanced photoelectrochemical water splitting *Adv. Mater.* **28** 6405–10
[39] Cesar I, Kay A, Gonzalez Martinez J A and Grätzel M 2006 Translucent thin film Fe_2O_3 photoanodes for efficient water splitting by sunlight: nanostructure-directing effect of Si-doping *J. Am. Chem. Soc.* **128** 4582–3
[40] Kennedy J H and Frese K W Jr 1978 Photo-oxidation of water at alpha-Fe_2O_3 electrode *J. Electrochem. Soc.* **125** 709–14
[41] Nakashima S, Negishi R and Tada H 2016 Visible-light-induced water oxidation by a hybrid photocatalyst consisting of bismuth vanadate and copper(ii) meso-tetra(4-carboxyphenyl)porphyrin *Chem. Commun.* **52** 3665–8
[42] Tilley S D, Cornuz M, Sivula K and Grätzel M 2010 Light-inducedwater splitting with hematite: improved nanostructure and iridium oxide catalysis *Angew. Chem., Int. Ed. Engl.* **49** 6405–8
[43] Cummings C Y, Marken F, Peter L M, Tahir A A and Wijayantha K G U 2012 Kinetics and mechanism of light-driven oxygen evolution at thin film α-Fe_2O_3 electrodes *Chem. Commun.* **48** 2027–9
[44] Barroso M, Pendlebury S R, Cowan A J and Durrant J R 2013 Charge carrier trapping, recombination and transfer in hematite (α-Fe_2O_3) water splitting photoanodes *Chem. Sci.* **4** 2724–34
[45] Annamalai A, Shinde P S, Jeon T H, Lee H H, Kim H G, Choi W and Jang J S 2016 Fabrication of superior α-Fe_2O_3 nanorod photoanodes through ex-situ Sn-doping for solar water splitting *Sol. Energy Mater. Sol. Cells* **144** 247–55
[46] Warren S C, Voïtchovsky K, Dotan H, Leroy C M, Cornuz M, Stellacci F, Hébert C, Rothschild A and Grätzel M 2013 Identifying champion nanostructures for solar water-splitting *Nat. Mater.* **12** 842–9
[47] Dayal G, Chiam S Y, Kumar M H, Bassi P S, Seng H L, Barber J and Wong L H 2014 Improving the efficiency of hematite nanorods for photoelectrochemical water splitting by doping with manganese *ACS Appl. Mater. Interfaces* **6** 5852–9
[48] Luo Z, Wang T, Zhang J, Li C, Li H and Gong J 2017 Dendritic hematite nanoarray photoanode modified with a conformal titanium dioxide interlayer for effective charge collection *Angew. Chem., Int. Ed. Engl.* **56** 12878–82
[49] Dlugosch T, Chnani A, Muralidhar P, Schirmer A, Biskupek J and Strehle S 2017 Thermal oxidation synthesis of crystalline iron-oxide nanowires on low-cost steel substrates for solar water splitting *Semicond. Sci. Technol.* **32** 084001
[50] Balko B A and Clarkson K M 2001 The effect of doping with Ti(IV) and Sn(IV) on oxygen reduction at hematite electrodes *J. Electrochem. Soc.* **148** E85–91
[51] Zhou Z, Huo P, Guo L and Prezhdo O V 2015 Understanding hematite doping with group IV elements: a DFT+U study *J. Phys. Chem.* C **119** 26303–10
[52] Liao P, Toroker M C and Carter E A 2011 Electron transport in pure and doped hematite. *Nano Lett.* **11** 1775–81
[53] Liao P and Carter E A 2012 Hole transport in pure and doped hematite *J. Appl. Phys.* **112** 013701
[54] Gardner R F G, Sweett F and Tanner D W 1963 The electrical properties of alpha ferric oxide—II.: ferric oxide of high purity *J. Phys. Chem. Solids* **24** 1183–96
[55] Iordanova N, Dupuis M and Rosso K M 2005 Charge transport in metal oxides: a theoretical study of hematite α-Fe_2O_3 *J. Chem. Phys.* **122** 144305
[56] Deng J, Zhong J, Pu A, Zhang D, Li M, Sun X and Lee S-T 2012 Ti-doped hematite nanostructures for solar water splitting with high efficiency *J. Appl. Phys.* **112** 084312
[57] Kumar P, Sharma P, Shrivastav R, Dass S and Satsangi V R 2011 Electrodeposited zirconium-doped α-Fe_2O_3 thin film for photoelectrochemical water splitting *Int. J. Hydrog. Energy* **36** 2777–84
[58] Bora D K 2015 Fabrication of silicon doped hematite photoelectrode with enhanced photocurrent density via solution processing of an *in situ* TEOS modified precursor *Mater. Sci. Semicond. Process.* **31** 728–38
[59] Mohapatra M, Padhi T, Anand S and Mishra B K 2012 CTAB mediated Mg-doped nano Fe_2O_3: synthesis, characterization, and fluoride adsorption behavior *Desalination Water Treat.* **50** 376–86
[60] Meng X Y, Qin G W, Li S, Wen X H, Ren Y P, Pei W L and Zuo L 2011 Enhanced photoelectrochemical activity for Cu and Ti doped hematite: the first principles calculations *Appl. Phys. Lett.* **98** 112104
[61] Cheng W *et al* 2012 Ni-doped overlayer hematite nanotube: a highly photoactive architecture for utilization of visible light *J. Phys. Chem.* C **116** 24060–7
[62] Annamalai A, Lee H H, Choi S H, Lee S Y, Gracia-Espino E, Subramanian A, Park J, Kong K-J and Jang J S 2016 Sn/Be sequentially co-doped hematite photoanodes for enhanced photoelectrochemical water oxidation: effect of Be^{2+} as co-dopant *Sci. Rep.* **6** 23183
[63] Ling Y and Li Y 2014 Review of Sn-doped hematite nanostructures for photoelectrochemical water splitting *Part. Part. Syst. Charact.* **31** 1113–21
[64] Xi L, Chiam S Y, Mak W F, Tran P D, Barber J, Loo S C J and Wong L H 2013 A novel strategy for surface treatment on hematite photoanode for efficient water oxidation *Chem. Sci.* **4** 164–9

[65] Ling Y, Wang G, Wheeler D A, Zhang J Z and Li Y 2011 Sn-doped hematite nanostructures for photoelectrochemical water splitting *Nano Lett.* **11** 2119–25
[66] Steier L, Herraiz-Cardona I, Gimenez S, Fabregat-Santiago F, Bisquert J, Tilley S D and Grätzel M 2014 Understanding the role of underlayers and overlayers in thin film hematite photoanodes *Adv. Funct. Mater.* **24** 7681–8
[67] Wang G, Ling Y, Wheeler D A, George K E N, Horsley K, Heske C, Zhang J Z and Li Y 2011 Facile synthesis of highly photoactive α-Fe_2O_3-based films for water oxidation *Nano Lett.* **11** 3503–9
[68] Cesar I, Sivula K, Kay A, Zboril R and Grätzel M 2009 Influence of feature size, film thickness, and silicon doping on the performance of nanostructured hematite photoanodes for solar water splitting *J. Phys. Chem.* C **113** 772–82
[69] Hu Y, Bora D K, Boudoire F, Häussler F, Graetzel M, Constable E C and Braun A 2013 A dip coating process for large area silicon-doped high performance hematite photoanodes *J. Renew. Sustain. Energy* **5** 043109
[70] Wang D, Chen H, Chang G, Lin X, Zhang Y, Aldalbahi A, Peng C, Wang J and Fan C 2015 Uniform doping of titanium in hematite nanorods for efficient photoelectrochemical water splitting *ACS Appl. Mater. Interfaces* **7** 14072–8
[71] Hahn N T and Mullins C B 2010 Photoelectrochemical performance of nanostructured Ti- and Sn-doped α-Fe_2O_3 photoanodes *Chem. Mater.* **22** 6474–82
[72] Zhang P, Kleiman-Shwarsctein A, Hu Y-S, Lefton J, Sharma S, Forman A J and McFarland E 2011 Oriented Ti doped hematite thin film as active photoanodes synthesized by facile APCVD *Energy Environ. Sci.* **4** 1020–8
[73] Cho I S, Han H S, Logar M, Park J and Zheng X 2016 Enhancing low-bias performance of hematite photoanodes for solar water splitting by simultaneous reduction of bulk, interface, and surface recombination pathways *Adv. Energy Mater.* **6** 1501840
[74] Liu J, Cai Y Y, Tian Z F, Ruan G S, Ye Y X, Liang C H and Shao G S 2014 Highly oriented Ge-doped hematite nanosheet arrays for photoelectrochemical water oxidation *Nano Energy* **9** 282–90
[75] Wang L, Lee C-Y, Mazare A, Lee K, Müller J, Spiecker E and Schmuki P 2014 Enhancing the water splitting efficiency of Sn-doped hematite nanoflakes by flame annealing *Chemistry* A **20** 77–82
[76] Le Formal F, Tetreault N, Cornuz M, Moehl T, Gratzel M and Sivula K 2011 Passivating surface states on water splitting hematite photoanodes with alumina overlayers *Chem. Sci.* **2** 737–43
[77] Ahmed M G, Kretschmer I E, Kandiel T A, Ahmed A Y, Rashwan F A and Bahnemann D W A 2015 Facile surface passivation of hematite photoanodes with TiO_2 overlayers for efficient solar water splitting *ACS Appl. Mater. Interfaces* **7** 24053–62
[78] Wang Z, Liu G, Ding C, Chen Z, Zhang F, Shi J and Li C 2015 Synergetic effect of conjugated $Ni(OH)_2/IrO_2$ cocatalyst on titanium-doped hematite photoanode for solar water splitting *J. Phys. Chem.* C **119** 19607–12
[79] Zhong D K, Cornuz M, Sivula K, Gratzel M and Gamelin D R 2011 Photo-assisted electrodeposition of cobalt–phosphate (Co–Pi) catalyst on hematite photoanodes for solar water oxidation *Energy Environ. Sci.* **4** 1759–64
[80] Morales-Guio C G, Mayer M T, Yella A, Tilley S D, Grätzel M and Hu X 2015 An optically transparent iron nickel oxide catalyst for solar water splitting *J. Am. Chem. Soc.* **137** 9927–36
[81] Goncalves R H and Leite E R 2014 The colloidal nanocrystal deposition process: an advanced method to prepare high performance hematite photoanodes for water splitting *Energy Environ. Sci.* **7** 2250–4
[82] Kay A, Cesar I and Grätzel M 2006 New benchmark for water photooxidation by nanostructured α-Fe_2O_3 films *J. Am. Chem. Soc.* **128** 15714–21
[83] Kaouk A, Ruoko T-P, Pyeon M, Gönüllü Y, Kaunisto K, Lemmetyinen H and Mathur S 2016 High water-splitting efficiency through intentional In and Sn codoping in hematite photoanodes *J. Phys. Chem.* C **120** 28345–53
[84] Brillet J, Grätzel M and Sivula K 2010 Decoupling feature size and functionality in solution-processed, porous hematite electrodes for solar water splitting *Nano Lett.* **10** 4155–60
[85] Li H, Zhao Q D, Li X Y, Shi Y and Chen G H 2012 Fabrication and surface photovoltage study of hematite microparticles with hollow spindle-shaped structure *Appl. Surf. Sci.* **258** 7099–104
[86] Kleiman-Shwarsctein A, Huda M N, Walsh A, Yan Y, Stucky G D, Hu Y-S, Al-Jassim M M and McFarland E W 2010 Electrodeposited aluminum-doped α-Fe_2O_3 photoelectrodes: experiment and theory *Chem. Mater.* **22** 510–7
[87] Hisatomi T, Dotan H, Stefik M, Sivula K, Rothschild A, Grätzel M and Mathews N 2012 Enhancement in the performance of ultrathin hematite photoanode for water splitting by an oxide underlayer *Adv. Mater.* **24** 2699–702
[88] Zhang X, Li H, Wang S, Fan F-R F and Bard A J 2014 Improvement of hematite as photocatalyst by doping with tantalum *J. Phys. Chem.* C **118** 16842–50
[89] Shen S, Jiang J, Guo P, Kronawitter C X, Mao S S and Guo L 2012 Effect of Cr doping on the photoelectrochemical performance of hematite nanorod photoanodes *Nano Energy* **1** 732–41
[90] Zhang Y, Jiang S, Song W, Zhou P, Ji H, Ma W, Hao W, Chen C and Zhao J 2015 Nonmetal P-doped hematite photoanode with enhanced electron mobility and high water oxidation activity *Energy Environ. Sci.* **8** 1231–6
[91] Hisatomi T, Le Formal F, Cornuz M, Brillet J, Tetreault N, Sivula K and Gratzel M 2011 Cathodic shift in onset potential of solar oxygen evolution on hematite by 13-group oxide overlayers *Energy Environ. Sci.* **4** 2512–5
[92] Barroso M, Mesa C A, Pendlebury S R, Cowan A J, Hisatomi T, Sivula K, Grätzel M, Klug D R and Durrant J R 2012 Dynamics of photogenerated holes in surface modified α-Fe_2O_3 photoanodes for solar water splitting *Proc. Natl Acad. Sci.* **109** 15640–5
[93] Jang J-W *et al* 2015 Enabling unassisted solar water splitting by iron oxide and silicon *Nat Commun.* **6** 7447
[94] Klahr B, Gimenez S, Fabregat-Santiago F, Bisquert J and Hamann T W 2012 Photoelectrochemical and impedance spectroscopic investigation of water oxidation with 'Co–Pi'-coated hematite electrodes *J. Am. Chem. Soc.* **134** 16693–700
[95] Dayal G, Jeong D, Jin K, Ahn H-Y, Boix P P, Abdi F F, Mathews N, Nam K T and Wong L H 2016 Highly active MnO catalysts integrated onto Fe_2O_3 nanorods for efficient water splitting *Adv. Mater. Interfaces* **3** 1600176
[96] Kanan M W and Nocera D G 2008 *In situ* formation of an oxygen-evolving catalyst in neutral water containing phosphate and Co^{2+} *Science* **321** 1072–5
[97] Xi L, Tran P D, Chiam S Y, Bassi P S, Mak W F, Mulmudi H K, Batabyal S K, Barber J, Loo J S C and Wong L H 2012 Co_3O_4-decorated hematite nanorods as an effective photoanode for solar water oxidation *J. Phys. Chem.* C **116** 13884–9
[98] Kim D H *et al* 2016 Toward high-performance hematite nanotube photoanodes: charge-transfer engineering at heterointerfaces *ACS Appl. Mater. Interfaces* **8** 23793–800
[99] Zhong D K and Gamelin D R 2010 Photoelectrochemical water oxidation by cobalt catalyst ('Co–Pi')/α-Fe_2O_3

composite photoanodes: oxygen evolution and resolution of a kinetic bottleneck *J. Am. Chem. Soc.* **132** 4202–7

[100] McAlpin J G, Surendranath Y, Dincă M, Stich T A, Stoian S A, Casey W H, Nocera D G and Britt R D 2010 EPR evidence for Co(IV) species produced during water oxidation at neutral pH *J. Am. Chem. Soc.* **132** 6882–3

[101] Kanan M W, Yano J, Surendranath Y, Dincă M, Yachandra V K and Nocera D G 2010 Structure and valency of a cobalt–phosphate water oxidation catalyst determined by *in situ* x-ray spectroscopy *J. Am. Chem. Soc.* **132** 13692–701

[102] Surendranath Y, Kanan M W and Nocera D G 2010 Mechanistic studies of the oxygen evolution reaction by a cobalt–phosphate catalyst at neutral pH *J. Am. Chem. Soc.* **132** 16501–9

[103] Guan J, Li D, Si R, Miao S, Zhang F and Li C 2017 Synthesis and demonstration of subnanometric iridium oxide as highly efficient and robust water oxidation catalyst *ACS Catal.* **7** 5983–6

[104] Dayal G, Bullock J, Sranko D F, Towle C M, Lum Y, Hettick M, Scott M C, Javey A and Ager J 2017 Efficient solar-driven electrochemical CO_2 reduction to hydrocarbons and oxygenates *Energy Environ. Sci.* **10** 2222–30

[105] Trotochaud L, Young S L, Ranney J K and Boettcher S W 2014 Nickel–iron oxyhydroxide oxygen-evolution electrocatalysts: the role of intentional and incidental iron incorporation *J. Am. Chem. Soc.* **136** 6744–53

[106] Qi J, Zhang W, Xiang R, Liu K, Wang H-Y, Chen M, Han Y and Cao R 2015 Porous nickel–iron oxide as a highly efficient electrocatalyst for oxygen evolution reaction *Adv. Sci.* **2** 1500199

[107] Yin S, Tu W, Sheng Y, Du Y, Kraft M, Borgna A and Xu R 2018 A highly efficient oxygen evolution catalyst consisting of interconnected nickel–iron-layered double hydroxide and carbon nanodomains *Adv. Mater.* **30** 1705106

[108] Li X L, Bassi P S, Boix P P, Fang Y N and Wong L H 2015 Revealing the role of TiO_2 surface treatment of hematite nanorods photoanodes for solar water splitting *ACS Appl. Mater. Interfaces* **7** 16960–6

[109] Dayal G, Chee P M, Boix P P, Ge H, Yanan F, Barber J and Wong L H 2015 Core–shell hematite nanorods: a simple method to improve the charge transfer in the photoanode for photoelectrochemical water splitting *ACS Appl. Mater. Interfaces* **7** 6852–9

[110] Yang X, Liu R, Du C, Dai P, Zheng Z and Wang D 2014 Improving hematite-based photoelectrochemical water splitting with ultrathin TiO_2 by atomic layer deposition *ACS Appl. Mater. Interfaces* **6** 12005–11

[111] Ahn H-J, Yoon K-Y, Kwak M-J and Jang J-H 2016 A titanium-doped SiO_x passivation layer for greatly enhanced performance of a hematite-based photoelectrochemical system *Angew. Chem., Int. Ed. Engl.* **55** 9922–6

[112] Xi L, Bassi P S, Chiam S Y, Mak W F, Tran P D, Barber J, Chye Loo J S and Wong L H 2012 Surface treatment of hematite photoanodes with zinc acetate for water oxidation *Nanoscale* **4** 4430–3

[113] Zhang P, Wang T, Chang X, Zhang L and Gong J 2016 Synergistic cocatalytic effect of carbon nanodots and Co_3O_4 nanoclusters for the photoelectrochemical water oxidation on hematite *Angew. Chem., Int. Ed. Engl.* **55** 5851–5

[114] Hu Y-S, Kleiman-Shwarsctein A, Stucky G D and McFarland E W 2009 Improved photoelectrochemical performance of Ti-doped α-Fe_2O_3 thin films by surface modification with fluoride *Chem. Commun.* **0** 2652–4

[115] Zhong D K, Sun J, Inumaru H and Gamelin D R 2009 Solar water oxidation by composite catalyst/α-Fe_2O_3 photoanodes *J. Am. Chem. Soc.* **131** 6086–7

[116] Kim J Y, Youn D H, Kang K and Lee J S 2016 Highly conformal deposition of an ultrathin FeOOH layer on a hematite nanostructure for efficient solar water splitting *Angew. Chem., Int. Ed. Engl.* **55** 10854–8

[117] Young K M H and Hamann T W 2014 Enhanced photocatalytic water oxidation efficiency with $Ni(OH)_2$ catalysts deposited on α-Fe_2O_3 via ALD *Chem. Commun.* **50** 8727–30

[118] Hong Y-R, Liu Z, Fatanah S, Al-Bukhari B S A, Lee C J J, Yung D L, Chi D and Hor T S A 2011 Effect of oxygen evolution catalysts on hematite nanorods for solar water oxidation *Chem. Commun.* **47** 10653–5

[119] Peter L M 1990 Dynamic aspects of semiconductor photoelectrochemistry *Chem. Rev.* **90** 753–69

[120] Dunn H K, Feckl J M, Muller A, Fattakhova-Rohlfing D, Morehead S G, Roos J, Peter L M, Scheu C and Bein T 2014 Tin doping speeds up hole transfer during light-driven water oxidation at hematite photoanodes *Phys. Chem. Chem. Phys.* **16** 24610–20

[121] Dayal G, Peter L M, Wong L H and Abdi F F 2017 Revealing the influence of doping and surface treatment on the surface carrier dynamics in hematite nanorod photoanodes *ACS Appl. Mater. Interfaces* **9** 41265–72

[122] Thorne J E, Jang J-W, Liu E Y and Wang D 2016 Understanding the origin of photoelectrode performance enhancement by probing surface kinetics *Chem. Sci.* **7** 3347–54

[123] Abdi F F and Berglund S P 2017 Recent developments in complex metal oxide photoelectrodes *J. Phys. D: Appl. Phys.* **50** 193002

[124] Gao X M, Li M W, Hou Y L and Wang C Y 2015 Characterisation of Fe_2TiO_5 nanocrystallites synthesised via homogeneous precipitation *Mater. Res. Innovations* **19** 1–6

[125] Gupta S K, Rajakumar V and Grieveson P 1991 Phase-transformations during heating of ilmenite concentrates *Metall. Trans.* B **22** 711–6

[126] Seitz G, Penin N, Decoux L, Wattiaux A, Duttine M and Gaudon M 2016 Near the ferric pseudobrookite composition (Fe_2TiO_5) *Inorg. Chem.* **55** 2499–507

[127] Iwauchi K, Yamamoto S, Bando Y, Hanai T, Koizumi N, Takada T and Fukushima S 1971 Dielectric properties of mixttures of Alpha-Fe_2O_3, TiO_2 and Fe_2TiO_5 *Japan. J. Appl. Phys.* **10** 1513

[128] Muranaka S, Shinjo T, Bando Y and Takada T 1971 Mossbauer study of Fe_2TiO_5 and $FeTi_2O_5$ *J. Phys. Soc. Japan* **30** 890

[129] Ginley D S and Baughman R J 1976 Preparation and czochralski crystal-growth of iron titanates, $FeTiO_3$, Fe_2TiO_4, and Fe_2TiO_5 *Mater. Res. Bull.* **11** 1539–43

[130] Nikolic M V, Sekulic D L, Vasiljevic Z Z, Lukovic M D, Pavlovic V B and Aleksic O S 2017 Dielectric properties, complex impedance and electrical conductivity of Fe_2TiO_5 nanopowder compacts and bulk samples at elevated temperatures *J. Mater. Sci.* **28** 4796–806

[131] Sharma S, Basu T, Shahee A, Singh K, Lalla N P and Sampathkumaran E V 2016 Complex dielectric and impedance behavior of magnetoelectric Fe_2TiO_5 *J. Alloys Compd.* **663** 289–94

[132] Guo W Q, Malus S, Ryan D H and Altounian Z 1999 Crystal structure and cation distributions in the $FeTi_2O_5$–Fe_2TiO_5 solid solution series *J. Phys.:Condens. Matter* **11** 6337–46

[133] Yu R, Li Z, Wang D, Lai X, Xing C, Yangb M and Xing X 2010 Fe_2TiO_5/alpha-Fe_2O_3 nanocomposite hollow spheres with enhanced gas-sensing properties *Scr. Mater.* **63** 155–8

[134] Iwauchi K and Ikeda Y 1990 Magnetic-properties of sintered Fe_2TiO_5 *Phys. Status Solidi* a **119** K71–4
[135] Khanahmadzadeh S and Salek S 2014 Fabrication, thermal, and magnetic properties of Fe_2TiO_5/polyaniline nanocomposites *Synth. React. Inorg. Met-Org. Nano-Met. Chem.* **44** 719–23
[136] Enhessari M, Razi M K, Etemad L, Parviz A and Sakhaei M 2014 Structural, optical and magnetic properties of the Fe_2TiO_5 nanopowders *J. Exp. Nanosci.* **9** 167–76
[137] Xiong K, Wang K Z, Chen L, Wang X Q, Fan Q B, Courtois J, Liu Y L, Tuo X G and Yan M H 2018 Heterostructured $ZnFe_2O_4$/Fe_2TiO_5/TiO_2 composite nanotube arrays with an improved photocatalysis degradation efficiency under simulated sunlight irradiation *Nano-Micro Lett.* **10** 17
[138] Khanahmadzadeh S and Hosseiny G 2016 Synthesis, characterization, and thermal properties of Fe_2TiO_5/cellulose and cellulose acetate nanocomposites *Synth. React. Inorg. Met-Org. Nano-Met. Chem.* **46** 713–7
[139] Gao Q, Wu X M, Fan Y M and Meng Q L 2017 Color performance and near infrared reflectance property of novel yellow pigment based on Fe_2TiO_5 nanorods decorated mica composites *Dyes Pigments* **146** 537–42
[140] Phani A R, Ruggieri F, Passacantando M and Santucci S 2008 Low temperature growth of nanocrystalline Fe_2TiO_5 perovskite thin films by sol-gel process assisted by microwave irradiation *Ceram. Int.* **34** 205–11
[141] Min K M, Park K S, Lim A H, Kim J C and Kim D W 2012 Synthesis of pseudobrookite-type Fe_2TiO_5 nanoparticles and their Li-ion electroactivity *Ceram. Int.* **38** 6009–13
[142] Guo S M, Wang S Y, Wu N N, Liu J R, Ni Y X and Liu W 2015 Facile synthesis of porous Fe_2TiO_5 microparticulates serving as anode material with enhanced electrochemical performances *RSC Adv.* **5** 103767–75
[143] Ku Y, Liu Y C, Chiu P C, Kuo Y L and Tseng Y H 2014 Mechanism of Fe_2TiO_5 as oxygen carrier for chemical looping process and evaluation for hydrogen generation *Ceram. Int.* **40** 4599–605
[144] Deng J J, Lv X X, Liu J Y, Zhang H, Nie K Q, Hong C H, Wang J O, Sun X H, Zhong J and Lee S T 2015 Thin-layer Fe_2TiO_5 on hematite for efficient solar water oxidation *ACS Nano* **9** 5348–56
[145] An X Q, Lan H C, Liu R P, Liu H J and Qu J H 2017 Light absorption modulation of novel Fe_2TiO_5 inverse opals for photoelectrochemical water splitting *New J. Chem.* **41** 7966–71
[146] Zhang H, Kim J H, Kim J H and Lee J S 2017 Engineering highly ordered iron titanate nanotube array photoanodes for enhanced solar water splitting activity *Adv. Funct. Mater.* **27** 1702428
[147] Shen S H, Lindley S A, Chen X Y and Zhang J Z 2016 Hematite heterostructures for photoelectrochemical water splitting: rational materials design and charge carrier dynamics *Energy Environ. Sci.* **9** 2744–75
[148] Liu Q H *et al* 2014 Aligned Fe_2TiO_5-containing nanotube arrays with low onset potential for visible-light water oxidation *Nat. Commun.* **5** 5122
[149] Li J T and Wu N Q 2015 Semiconductor-based photocatalysts and photoelectrochemical cells for solar fuel generation: a review *Catal. Sci. Technol.* **5** 1360–84
[150] Waqas M, Iqbal S, Bahadur A, Saeed A, Raheel M and Javed M 2017 Designing of a spatially separated hetero-junction pseudobrookite (Fe_2TiO_5–TiO_2) yolk-shell hollow spheres as efficient photocatalyst for water oxidation reaction *Appl. Catal.* B **219** 30–5
[151] Waqas M, Wei Y Z, Mao D, Qi J, Yang Y, Wang B and Wang D 2017 Multi-shelled TiO_2/Fe_2TiO_5 heterostructured hollow microspheres for enhanced solar water oxidation *Nano Res.* **10** 3920–8
[152] Courtin E, Baldinozzi G, Sougrati M T, Stievano L, Sanchez C and Laberty-Robert C 2014 New Fe_2TiO_5-based nanoheterostructured mesoporous photoanodes with improved visible light photoresponses *J. Mater. Chem.* A **2** 6567–77
[153] Lin Y G, Hsu Y K, Lin Y C and Chen Y C 2016 Electrodeposited Fe_2TiO_5 nanostructures for photoelectrochemical oxidation of water *Electrochim. Acta* **213** 898–903
[154] Bassi P S, Antony R P, Boix P P, Fang Y N, Barber J and Wong L H 2016 Crystalline Fe_2O_3/Fe_2TiO_5 heterojunction nanorods with efficient charge separation and hole injection as photoanode for solar water oxidation *Nano Energy* **22** 310–8
[155] Wang L, Nguyen N T and Schmuki P 2016 A facile surface passivation of hematite photoanodes with iron titanate cocatalyst for enhanced water splitting *Chemsuschem* **9** 2048–53
[156] Li C C, Wang T, Luo Z B, Liu S S and Gong J L 2016 Enhanced charge separation through ALD-modified Fe_2O_3/Fe_2TiO_5 nanorod heterojunction for photoelectrochemical water oxidation *Small* **12** 3415
[157] Wang L, Nguyen N T, Huang X J, Schmuki P and Bi Y P 2017 Hematite photoanodes: synergetic enhancement of light harvesting and charge management by sandwiched with Fe_2TiO_5/Fe_2O_3/Pt structures *Adv. Funct. Mater.* **27** 1703527
[158] Lv X L, Nie K Q, Lan H W, Li X, Li Y Y, Sun X H, Zhong J and Lee S T 2017 Fe_2TiO_5-incorporated hematite with surface P-modification for high-efficiency solar water splitting *Nano Energy* **32** 526–32
[159] Deng J J, Lv X X, Nie K Q, Lv X L, Sun X H and Zhong J 2017 Lowering the onset potential of Fe_2TiO_5/Fe_2O_3 photoanodes by interface structures: F- and Rh-based treatments *ACS Catal.* **7** 4062–9
[160] Tang P Y *et al* 2017 Enhanced photoelectrochemical water splitting of hematite multilayer nanowire photoanodes by tuning the surface state via bottom-up interfacial engineering *Energy Environ. Sci.* **10** 2124–36
[161] Chen S, Zeng Q Y, Bai J, Li J H, Li L S, Xia L G and Zhou B X 2017 Preparation of hematite with an ultrathin iron titanate layer via an *in situ* reaction and its stable, long-lived, and excellent photoelectrochemical performance *Appl. Catal.* B **218** 690–9
[162] Deng Y X, Xing M Y and Zhang J L 2017 An advanced TiO_2/Fe_2TiO_5/Fe_2O_3 triple-heterojunction with enhanced and stable visible-light-driven fenton reaction for the removal of organic pollutants *Appl. Catal.* B **211** 157–66
[163] Ruoko T P, Kaunisto K, Bartsch M, Pohjola J, Hiltunen A, Niederberger M, Tkachenko N V and Lemmetyinen H 2015 Subpicosecond to second time-scale charge carrier kinetics in hematite-titania nanocomposite photoanodes *J. Phys. Chem. Lett.* **6** 2859–64
[164] Monllor-Satoca D, Bartsch M, Fabrega C, Genc A, Reinhard S, Andreu T, Arbiol J, Niederberger M and Morante J R 2015 What do you do, titanium? Insight into the role of titanium oxide as a water oxidation promoter in hematite-based photoanodes *Energy Environ. Sci.* **8** 3242–54
[165] Hussain S, Hussain S, Waleed A, Tavakoli M M, Yang S H, Rauf M K, Fan Z Y and Nadeem M A 2017 Spray pyrolysis deposition of $ZnFe_2O_4$/Fe_2O_3 composite thin films on hierarchical 3D nanospikes for efficient photoelectrochemical oxidation of water *J. Phys. Chem.* C **121** 18360–8
[166] Miao C H, Ji S L, Xu G P, Liu G D, Zhang L D and Ye C H 2012 Micro-nano-structured Fe_2O_3:Ti/$ZnFe_2O_4$

heterojunction films for water oxidation *ACS Appl. Mater. Interfaces* **4** 4428–33
[167] Hou Y, Zuo F, Dagg A and Feng P Y A 2013 Three-dimensional branched cobalt-doped alpha-Fe_2O_3 nanorod/$MgFe_2O_4$ heterojunction array as a flexible photoanode for efficient photoelectrochemical water oxidation *Angew. Chem., Int. Ed. Engl.* **52** 1248–52
[168] Ahmed M G, Kandiel T A, Ahmed A Y, Kretschmer I, Rashwan F and Bahnemann D 2015 Enhanced photoelectrochemical water oxidation on nanostructured hematite photoanodes via p-$CaFe_2O_4$/n-Fe_2O_3 heterojunction formation *J. Phys. Chem.* C **119** 5864–71
[169] Guo Y H, Fu Y M, Liu Y and Shen S H 2014 Photoelectrochemical activity of $ZnFe_2O_4$ modified alpha-Fe_2O_3 nanorod array films *RSC Adv.* **4** 36967–72
[170] Wang Q Y, Liu Z D, Lu Q F, Guo E Y and Wei M Z 2018 Fabrication of direct Z-scheme alpha-Fe_2O_3/$FeVO_4$ nanobelts with enhanced photoelectrochemical performance *Chem. Select* **3** 809–15
[171] Zhang M Y, Ma Y M, Friedrich D, van de Krol R, Wong L H and Abdi F F 2018 Elucidation of the opto-electronic and photoelectrochemical properties of $FeVO_4$ photoanodes for solar water oxidation *J. Mater. Chem.* A **6** 548–55
[172] Li J H, Han M S, Guo Y, Wang F and Sun C 2016 Fabrication of $FeVO_4$/Fe_2TiO_5 composite catalyst and photocatalytic removal of norfloxacin *Chem. Eng. J.* **298** 300–8
[173] Lin Y J, Xu Y, Mayer M T, Simpson Z I, McMahon G, Zhou S and Wang D W 2012 Growth of p-type hematite by atomic layer deposition and its utilization for improved solar water splitting *J. Am. Chem. Soc.* **134** 5508–11
[174] Lin Y, Zhou S, Sheehan S W and Wang D 2011 Nanonet-based hematite heteronanostructures for efficient solar water splitting *J. Am. Chem. Soc.* **133** 2398–401
[175] Young Kim J, Jang J-W, Hyun Youn D, Yul Kim J, Sun Kim E and Sung Lee J 2012 Graphene-carbon nanotube composite as an effective conducting scaffold to enhance the photoelectrochemical water oxidation activity of a hematite film *RSC Adv.* **2** 9415–22
[176] Chen Z, Ren W, Gao L, Liu B, Pei S and Cheng H-M 2011 Three-dimensional flexible and conductive interconnected graphene networks grown by chemical vapour deposition *Nat. Mater.* **10** 424
[177] Yoon K-Y, Lee J-S, Kim K, Bak C H, Kim S-I, Kim J-B and Jang J-H 2014 Hematite-based photoelectrochemical water splitting supported by inverse opal structures of graphene *ACS Appl. Mater. Interfaces* **6** 22634–9
[178] Meng F, Li J, Cushing S K, Bright J, Zhi M, Rowley J D, Hong Z, Manivannan A, Bristow A D and Wu N 2013 Photocatalytic water oxidation by hematite/reduced graphene oxide composites *ACS Catal.* **3** 746–51
[179] Pihosh Y *et al* 2015 Photocatalytic generation of hydrogen by core-shell WO_3/$BiVO_4$ nanorods with ultimate water splitting efficiency *Sci. Rep.* **5** 11141
[180] Riha S C, DeVries Vermeer M J, Pellin M J, Hupp J T and Martinson A B F 2013 Hematite-based photo-oxidation of water using transparent distributed current collectors *ACS Appl. Mater. Interfaces* **5** 360–7
[181] Lin Y, Yuan G, Sheehan S, Zhou S and Wang D 2011 Hematite-based solar water splitting: challenges and opportunities *Energy Environ. Sci.* **4** 4862–9
[182] Tamirat A G, Su W-N, Dubale A A, Pan C-J, Chen H-M, Ayele D W, Lee J-F and Hwang B-J 2015 Efficient photoelectrochemical water splitting using three dimensional urchin-like hematite nanostructure modified with reduced graphene oxide *J. Power Sources* **287** 119–28
[183] Liu Y, Wang D-P, Yu Y-X and Zhang W-D 2012 Preparation and photoelectrochemical properties of functional carbon nanotubes and Ti co-doped Fe_2O_3 thin films *Int. J. Hydrog. Energy* **37** 9566–75
[184] He L, Jing L, Luan Y, Wang L and Fu H 2014 Enhanced visible activities of α-Fe_2O_3 by coupling N-doped graphene and mechanism insight *ACS Catal.* **4** 990–8
[185] Hou Y, Zuo F, Dagg A and Feng P 2012 Visible light-driven α-Fe_2O_3 nanorod/graphene/$BiV_{1-x}Mo_xO_4$ core/shell heterojunction array for efficient photoelectrochemical water splitting *Nano Lett.* **12** 6464–73
[186] Xiaobo C, Haifeng Z and Chuanwei C 2017 3D FTO inverse opals@hematite@TiO_2 hierarchically structured photoanode for photoelectrochemical water splitting *Semicond. Sci. Technol.* **32** 114003
[187] Bolton J R, Strickler S J and Connolly J S 1985 Limiting and realizable efficiencies of solar photolysis of water *Nature* **316** 495–500
[188] Hu S, Xiang C, Haussener S, Berger A D and Lewis N S 2013 An analysis of the optimal band gaps of light absorbers in integrated tandem photoelectrochemical water-splitting systems *Energy Environ. Sci.* **6** 2984–93
[189] Brillet J, Cornuz M, Formal F L, Yum J-H, Grätzel M and Sivula K 2010 Examining architectures of photoanode–photovoltaic tandem cells for solar water splitting *J. Mater. Res.* **25** 17–24
[190] Zhang K, Ma M, Li P, Wang D H and Park J H 2016 Water splitting progress in tandem devices: moving photolysis beyond electrolysis *Adv. Energy Mater.* **6** 1600602
[191] Chen Y-S, Manser J S and Kamat P V 2015 All solution-processed lead halide perovskite-$BiVO_4$ tandem assembly for photolytic solar fuels production *J. Am. Chem. Soc.* **137** 974–81
[192] Brillet J, Yum J-H, Cornuz M, Hisatomi T, Solarska R, Augustynski J, Graetzel M and Sivula K 2012 Highly efficient water splitting by a dual-absorber tandem cell *Nat. Photon.* **6** 824–8
[193] Chae S Y, Park S J, Joo O-S, Min B K and Hwang Y J 2016 Spontaneous solar water splitting by DSSC/CIGS tandem solar cells *Solar Energy* **135** 821–6
[194] Park J H and Bard A J 2006 Photoelectrochemical tandem cell with bipolar dye-sensitized electrodes for vectorial electron transfer for water splitting *Electrochem. Solid-State Lett.* **9** E5–8
[195] Urbain F, Smirnov V, Becker J-P, Rau U, Ziegler J, Kaiser B, Jaegermann W and Finger F 2015 Application and modeling of an integrated amorphous silicon tandem based device for solar water splitting *Sol. Energy Mater. Sol. Cells* **140** 275–80
[196] Abdi F F, Han L, Smets A H M, Zeman M, Dam B and van de Krol R 2013 Efficient solar water splitting by enhanced charge separation in a bismuth vanadate-silicon tandem photoelectrode *Nat. Commun.* **4** 2195
[197] Lee M M, Teuscher J, Miyasaka T, Murakami T N and Snaith H J 2012 Efficient hybrid solar cells based on meso-superstructured organometal halide perovskites *Science* **338** 643–7
[198] Liu M, Johnston M B and Snaith H J 2013 Efficient planar heterojunction perovskite solar cells by vapour deposition *Nature* **501** 395–8
[199] Xing G, Mathews N, Sun S, Lim S S, Lam Y M, Grätzel M, Mhaisalkar S and Sum T C 2013 Long-range balanced electron- and hole-transport lengths in organic–inorganic $CH_3NH_3PbI_3$ *Science* **342** 344–7
[200] Cao Q, Yu J, Yuan K P, Zhong M and Delaunay J J 2017 Facile and large-area preparation of porous Ag_3PO_4 photoanodes for enhanced photoelectrochemical water oxidation *ACS Appl. Mater. Interfaces* **9** 19507–12